

The Optical Wind Line Variability of η Carinae During the 2009.0 Event¹

N. D. Richardson², D. R. Gies³, T. R. Gull⁴, A. F. J. Moffat², & L. St-Jean²

ABSTRACT

We report on high-resolution spectroscopy of the 2009.0 spectroscopic event of η Carinae collected via SMARTS observations using the CTIO 1.5 m telescope and echelle spectrograph. Our observations were made almost every night over a two-month interval around the photometric minimum of η Car associated with the periastron passage of a hot companion. The photoionizing flux of the companion and heating related to colliding winds causes large changes in the wind properties of the massive primary star. Here we present an analysis of temporal variations in a sample of spectral lines that are clearly formed in the wind of the primary star. These lines are affected by a changing illumination of the flux of the secondary star during the periastron passage. We document the sudden onset of blue-shifted absorption that occurred in most of the lines near or slightly after periastron, and we argue that these absorption components are seen when we view the relatively undisturbed wind of the foreground primary star. We present time series measurements of the net equivalent width of the wind lines and of the radial velocities of the absorption trough minima and the emission peak midpoints. Most lines decrease in emission strength around periastron, and

¹Based on observations taken at the Cerro Tololo Inter-American Observatory 1.5m telescope, National Optical Astronomy Observatory, which is operated by the Association of Universities for Research in Astronomy, under contract with the National Science Foundation.

²Département de physique and Centre de Recherche en Astrophysique du Québec (CRAQ), Université de Montréal, C.P. 6128, Succ. Centre-Ville, Montréal, Québec, H3C 3J7, Canada; richardson@astro.umontreal.ca

³Center for High Angular Resolution Astronomy, Department of Physics and Astronomy, Georgia State University, P. O. Box 5060, Atlanta, GA 30302–5060, USA

⁴Astrophysics Science Division, Code 667, NASA Goddard Space Flight Center, Greenbelt, MD 20771, USA

those high excitation lines formed close to the primary exhibit a red-ward velocity excursion. We show how these trends can be explained using an illuminated hemisphere model that is based on the idea that the emission originates primarily from the side of the primary facing the hot companion.

Subject headings: stars: early-type — stars: binaries — stars: winds, outflows — stars: individual (η Carinae)

1. Introduction

η Carinae A (HD 93308) is one of the most massive and luminous stars in the local region of the Galaxy. It is surrounded by an hourglass-shaped nebula called the Homunculus that was ejected during its mid-nineteenth century, luminous blue variable eruption (Davidson & Humphreys 1997). It is also the primary star in a 5.54 year, eccentric orbit with a hot, massive, binary companion (η Carinae B). Many properties of the observed flux are modulated with this 5.54 year periodicity (forbidden and permitted emission lines, e.g., Daminieli et al. 2000; photometric light curves, e.g., van Genderen et al. 2003, Fernández-Lajús et al. 2003, 2010, Whitelock et al. 2004; and X-ray light curves, e.g., Corcoran 2005) that is attributed to a highly eccentric ($e \sim 0.9$) binary orbit and changing illumination of the primary star’s wind and extended emission regions (Daminieli et al. 1997). The spectroscopic events and other rapid changes in flux occur near the periastron passages. An overview of the observational history is given in our previous paper on η Carinae (Richardson et al. 2010, hereafter Paper 1) as well as in Daminieli et al. (2008a,b).

The strongest constraints on the period of the binary system come from the X-ray light curve (e.g., Corcoran 2005; Corcoran et al. 2010) and the variability of the He II $\lambda 4686$ line (e.g., Mehner et al. 2011a; Teodoro et al. 2012), caused by the interaction of the winds of the two stars. X-rays from the wind–wind collision region encounter a varying column density of gas along our line of sight with the changing binary orientation. The X-ray maximum occurs shortly before periastron when the rarefied, highly ionized secondary star’s wind pushes much of the dense, partially ionized primary wind out of our line of sight (bounded by a Coriolis-deflected bow shock), while the X-ray minimum occurs close to periastron when the collision region is blocked by obscuring, dense gas of the primary’s wind. The He II variability shows some similarities to the X-ray flux variability and indicates formation in a hot plasma. Numerical models of the wind–wind collision by Okazaki et al. (2008) and Parkin et al. (2009) can reproduce many of the features of the X-ray light curve, but they also reveal discrepancies from observations made during the intense interaction at closest approach. Although the details of wind collision need further investigation, the basic geometry of the

models helps to explain the spatial variations of the emission spectrum from the resolved, extended wind region surrounding the central binary (Gull et al. 2009; Madura et al. 2012).

η Carinae is relatively nearby, situated in the Trumpler 16 cluster at a distance of 2.3 ± 0.1 kpc (Smith 2006), which has made it an excellent target for angularly resolved observations with the *Hubble Space Telescope* (HST) and the *Space Telescope Imaging Spectrograph* (STIS). With *HST/STIS*, we are able to probe structures to a spatial resolution of $0.1'' \approx 230$ AU in the system. Gull et al. (2009) demonstrate the complicated geometry of the system. Gull et al. (2011) show that the spatially resolved spectroscopy of η Car is best explained through colliding winds and provide 2-D models that explain the geometry of the different emission lines forming in the extended colliding-winds region. Madura et al. (2012) and Clementel et al. (2015a, 2015b) have further extended this modeling effort to show that the plane of the binary orbit is closely aligned to the plane of the Homunculus skirt, i.e., the bipolar ejecta of the Homunculus are nearly perpendicular to the binary plane. These models also show that η Car B passes behind η Car A’s thick wind across the observed minimum, consistent with the models of Okazaki et al. (2008).

The observed spectrum of η Car in the optical region is extremely complicated. There are emission lines from the nearby slow-moving ejecta, dominated by the Weigelt knots (Weigelt & Ebersberger 1986; Zethson et al. 2012). In addition, absorption lines from the Homunculus, Little Homunculus, and interstellar features complicate our understanding of the light emitted from the primary and secondary stars and their winds. Nielsen et al. (2009) presented a spectral atlas for the ultraviolet through near-infrared wavelength regions. In total, more than 1500 lines are present in the region between 3060 and 10430 Å, being formed in the ejecta, Weigelt knots, and the primary star’s wind. There is no known or measurable spectral contribution from the secondary star in this portion of the spectrum. In the optical, the primary wind has strong emission lines such as the hydrogen Balmer lines. Nielsen et al. (2007) showed that permitted transitions of He I, N II, Si II, and Fe II form in the wind of the primary star and the wind–wind collision zones. The wind lines tend to be extremely broad, and are typically observed to be mostly stable except during the spectroscopic events, when the emission line flux drops, and many lines develop P Cygni type absorptions. In addition, complex, broadened forbidden line emissions most noticeably of [Fe II], [Ni II], [N II] and [Fe III] are modulated across the 5.54 year period.

The variability of the optical spectrum is dominated by the 5.54 year orbit, with major changes happening near the periastron passage (the spectroscopic events) when the secondary enters the line forming region of the primary (Hillier et al. 2001). Nielsen et al. (2007) analyzed high spatial resolution spectroscopy obtained with the Hubble Space Telescope and found that the blue-shifted P Cygni absorption troughs of hydrogen, He I, and Fe II

were dependent on the orbital phase, with large blue-to-red Doppler shifts occurring during the periastron passages. They interpreted the radial velocity and strength variations to be caused by the interaction of the two stellar winds. Damini et al. (2008b) described the orbital variations of the spectrum in two stages. First, there is a slow variation due to changes in the ionization levels of the wind that are related to the changing binary separation. Then there is a rapid variation near periastron when the stars closely approach each other and cause a global collapse of the wind-wind collision shock zone. Mehner et al. (2011a) presented a detailed record of the spectral variations during the 2009 periastron event. Their Gemini GMOS observations recorded not only the spectral variations along the line of sight to the central binary, but also at four offset positions that record light scattered at different orientations to the binary. They found (along with Teodoro et al. 2012) that the He II $\lambda 4686$ emission displays a secondary peak after its collapse due to the geometry of the colliding winds. They also showed that the radial velocity variations of some lines were similar both along our line of sight to the system as well as from scattered light in the Homunculus thought to originate from a polar view of the star, and they suggested that the observed radial velocity variability is not related to binary motion.

In Paper 1, we presented our observations of H α over the 2009.0 event. We showed how the emission strength declined and blue-shifted absorption increased around the time of the X-ray minimum. These echelle spectroscopy observations recorded the spectrum between H β and approximately 7300 Å. In this paper, we present a more detailed look at the wind lines in order to provide a detailed account of the variations that occurred in this event and to consider explanations for them. In Section 2, we outline our observations and reductions. Section 3 details the profile morphologies through the event for H β , He I, N II, Na I D, Si II, and Fe II permitted lines. Section 4 details the kinematics and variability of the He I and other lines. In Section 5, we present a discussion focused on a simple model to understand the physics of the variability. We summarize our findings in Section 6.

2. Observations

We obtained high signal-to-noise observations with the CTIO 1.5m telescope and fiber-fed echelle spectrograph operated by the SMARTS Consortium ($R \sim 40,000$; Barden & Ingerson 1998) almost nightly during the 2009 spectroscopic minimum and periastron passage of η Car (a total of 40 spectra between 2008 Dec 18 and 2009 Feb 19). The reductions were described in Paper 1. Many of the spectra reported here had longer exposure times that saturated the H α profile but provide a higher signal to noise ratio for the other wind lines. We found that a 120s exposure would allow us to sample many of the wind lines in the

spectrum of η Car at a good signal to noise (usually at least a $S/N \approx 70$ – 100 per pixel in the wavelength range of ~ 4800 – 7200 Å), and we began making such exposures regularly after 2009 January 1. For this analysis, we constructed a telluric template spectrum based upon the observed spectrum of the O star μ Col obtained with the same spectrograph to identify features formed in Earth’s atmosphere. Most of the observed line profiles are relatively unaffected by such telluric absorption, but we corrected the line profiles of He I $\lambda 7065$ with the IRAF task `telluric`⁵.

We resumed monitoring the star roughly once per week with the same instrumentation in 2009 October, and this continued through 2010 (22 spectra between 2009 Oct 21 and 2010 Jun 12) when this echelle spectrograph was decommissioned in favor of a new echelle spectrograph. During this time, we continued making short exposures for $H\alpha$, and longer exposures (240 s) to obtain higher signal to noise for the other wind lines in the spectrum. The new camera system that was installed at the end of 2009 allowed us to extract an additional 17 orders of data in the blue (for 18 spectra). The new extractions extend the spectral coverage blueward to ~ 4000 Å, but the shortest wavelength regions have extremely low signal.

For comparative purposes, we include here one spectrum obtained with the CTIO 1.5 m telescope and its new echelle spectrograph CHIRON (Tokovinin et al. 2013), which was obtained near apastron on 2012 March 3. This observation had a signal-to-noise of ~ 150 per pixel, and a resolving power of 90,000. While the resolving power is much higher, we also note that the recorded spatial distribution of light on the sky is the same, because the new instrument uses the same fiber to input light into the spectrograph. We have continued our monitoring with CHIRON and these results will be shown in future analyses.

We note that there are several different definitions of phase for this system, which correspond to the different observable minima. We also note that none of these conventions necessarily relates to periastron passage. There is an X-ray minimum (Corcoran 2005), minima from different photometric filters in the ultraviolet through infrared wavelengths, a spectroscopically defined minimum (Damineli et al. 2008a) that corresponds to the time when the He I narrow emission from the Weigelt knots disappears, as well as a calendar based phase from the η Carinae Treasury Project⁶. While there is much debate over which phase is best to use (see the appendix of Mehner et al. 2011a), we adopt the spectroscopic

⁵IRAF is distributed by the National Optical Astronomy Observatory, which is operated by the Association of Universities for Research in Astronomy (AURA) under a cooperative agreement with the National Science Foundation.

⁶<http://etacar.umn.edu/>

definition of Damineli et al. (2008a) for this spectroscopic analysis. This corresponds to a zero point of HJD 2,452,819.8 (cycle 11) and a period of 2022.7 d, with the 2009 minimum occurring at HJD 2,454,842.5. The first recorded event where a major change was observed in the spectrum was event #1 in 1948 (Gaviola 1953), and the 2009.0 event corresponds to event #12 with this phase convention.

3. Wind-Line Morphologies During The 2009.0 Event

Our observations of η Carinae through the 2009.0 spectroscopic event recorded several permitted optical wind lines. In this section, we discuss observations of $H\beta$, as well as transitions of He I, N II, Si II, and Fe II. While our data set is rich in narrow emission lines originating in the Weigelt knots and ejecta, we focus here on the wind line developments during the event for this discussion. We present the rest wavelengths and atomic energy levels of the optical wind lines in Table 1. Table 1 includes the ionization energy of each species from a lower state and the lower and upper energy states of each transition compiled from NIST⁷ in Columns 1–4, the kinematic integration limits for equivalent widths. All the wind line variations are shown in the online Figure Set 1. Each entry of the figure set presents an image of the dynamical spectrum through the dense time sampling around periastron and line plots of representative spectra made before, during, and after the event. Arrows on the right hand side of the image indicate the actual times of observation while white line segments on the right hand side of the image indicate orbital phases 11.99, 12.00, and 12.01. The panel below the dynamical image plots the average spectrum. The panels for the line plots give (from bottom to top) sample spectra obtained before, during (with offsets related to time of observation), after periastron, and in 2012 with the CHIRON spectrograph. The individual plots are labeled with a date (HJD-2,450,000) and orbital phase ϕ . The corresponding figure numbers for each transition are given in column 8 of Table 1. Column 9 of Table 1 lists other features that blend with the line of interest and that complicate measurements. More complete listings of line blends can be found in the tables of Nielsen et al. (2009) and Zethson et al. (2012). Brief descriptions of the observed properties and variations follow in subsections for each line species.

⁷<http://nist.gov/pml/data/asd.cfm>

3.1. $H\beta$ and $H\alpha$

Our observations of the $H\beta$ profile during the 2009.0 event (Fig. Set 1.1) have lower signal to noise because the line is recorded in the low signal wings of the echelle blaze function, and consequently, the profiles are not of high enough quality to make reliable measurements (such as equivalent width or radial velocity) compared to the $H\alpha$ profiles (Paper 1). Nevertheless, these data do qualitatively show the same developments as seen in the $H\alpha$ line presented in Paper 1 (see Fig. Set 1.2). The anomalous narrow absorption component at $V_r = -144$ km s⁻¹, attributed to absorption from the Little Homunculus (Ishibashi et al. 2003), as well as a P Cygni type absorption both appear near HJD 2,454,837, just prior to phase 0.0. Mehner et al. (2011a) observed the $H\delta$ line during the 2009 event (see their Fig. 7), and it showed similar behavior of the P Cygni absorption component, but not in the narrow absorption, as $H\delta$ does not exhibit the narrow absorption component during the spectroscopic events. Curiously, the $H\delta$ profile observed at offset positions that record scattered light from higher stellar latitudes displays the P Cyg absorption continuously through the event rather than just appearing near the time of periastron.

3.2. He I Profiles

There are five He I lines ($\lambda\lambda 4921, 5016, 5876, 6678, \text{ and } 7065$ Å) present in the parts of our spectra with good signal-to-noise. All the lines are contaminated in some manner by blending with other emission or absorption lines. The 4921 and 5016 Å lines are blended with Fe II wind lines (Fig. Set 1.3, 1.4) that actually dominate the appearance and our measurements of the profiles (Zethson et al. 2012). The red wing of the 5876 line (Fig. Set 1.5) is blended with the complicated Na I D doublet (see Section 3.4), which has many absorption components from the intervening gas of the Homunculus, Little Homunculus, and interstellar gas, as well as emission from the wind of the primary (and possibly the secondary) star. The blue wing of this profile is blended with a weak [Fe II] $\lambda 5870$ emission line. The He I $\lambda 6678$ Å line has a [Ni II] line formed in the Weigelt knots on its blue wing, that interferes with the P Cygni absorption during the event (Fig. Set 1.6). The 7065 Å line (Fig. Set. 1.7) is rather clean in comparison, but the spectrum often has a large telluric component from the Earth’s atmosphere.

Fig. Set 1.5–1.7 display dynamical spectra and line plots of the He I $\lambda 5876, 6678, \text{ and } 7065$ profiles across the 2009.0 event. All these profiles show a fading and subsequent brightening in line emission, and the development of a strong P Cygni absorption component. He I $\lambda\lambda 5876, 6678, \text{ and } 7065$ Å lines all exhibit strong radial velocity shifts during the event, with a range of approximately 200 km s⁻¹. The lines all have a narrow emission component

(due to the Weigelt knots) that is present in early spectra, but disappears at phase 0.0 (by the definition of Daminieli et al. 2008a). The ephemeris of Daminieli et al. (2008a) is confirmed by these data as the narrow emission in the He I $\lambda 6678$ line disappears exactly at our observed phase 12.0.

Mehner et al. (2011a) discussed the behavior of He I $\lambda 4713$ during the 2009 spectroscopic event. They show that the equivalent width of the He I line rises in the months leading up to the event, with a fast decline near phase 0, and a short-lived increase after the minimum. Our results are very similar. Mehner et al. further describe the kinematics of feature, which are fully consistent with our kinematical measurements (Sections 4.2, 4.3).

3.3. N II Profiles

η Car is unique among the highest luminosity (and/or highest mass-loss rate) LBVs, in that N II $\lambda\lambda 5667$ – 5710 is very weak (e.g., Hillier et al. 2001). The comparison of η Carinae and HDE 316285 (Hillier et al. 2001) shows how strong these lines are in HDE 316285, but nearly absent in the spectrum of η Car. Fig. Set 1.8–1.10 present the dynamical spectra and line plots of the region of N II transitions. We had difficulties normalizing this region due to the large number of absorption and emission features, and a fairly small spectral window, caused by the narrow blaze function of the echelle spectrograph. We performed the normalizations by a localized fit of the data to smooth it, and then we fit a polynomial to regions we deemed to be continuum from the analysis of Mehner et al. (2011b). Similar difficulties were discussed in the analysis of Mehner et al. (2011b).

We observed three transitions in the echelle order best suited to the analysis of N II. The transitions at 5666, 5676, and 5710 Å always have some P Cygni type absorption present. The onset of deeper absorption is seen for the transitions at 5666, 5676, and 5710 Å just prior to phase zero, with the N II $\lambda 5676$ transition showing the deepest absorption for ≈ 5 days. All the N II profiles show a strong radial velocity shift from blue to red with a final reversal at the end of the observation run. From a visual inspection, the P Cygni type absorptions of N II (Fig. Set 1.8–1.10) are seen to show variations similar to those of the He I transitions (e.g., Fig. Set 1.6; He I $\lambda 6678$).

Mehner et al. (2011a) briefly discussed the N II multiplet at $\lambda\lambda 5666$ – 5710 in relation to the spectroscopic event, and showed how the direct view of the star and the view from position FOS4 (scattered light from the polar region) present similar line kinematics. Mehner et al. (2011b) extended the analysis and proposed that the variations were related to the changing illumination by the secondary star. They further state that these lines are the only

known features originating from the unperturbed primary wind.

3.4. Na I D profiles

The Na I D region is one of the most complex portions of the optical spectrum of η Car. In addition to the primary wind components, there is a blend of emission and several narrow absorption components from the intervening gas in the Homunculus and Little Homunculus in addition to interstellar absorption. Most of the narrow absorptions are from the great eruption of 1837-1860 (-512 km s^{-1}) or the lesser eruption of 1885-1895 (-146 km s^{-1}) and similar line absorption structure for UV resonance lines was described by Gull et al. (2006). An examination of the profiles (Fig. Set 1.11–1.12) shows that there are multiple velocity components between the extreme velocities of -512 and -146 km s^{-1} , as seen in ultraviolet resonance lines (Gull et al. 2005). Other LBVs show this resonance line as a P Cygni profile with both emission and absorption components from the stellar wind as well as the interstellar components. For example, the star HDE 316285 was observed to have such a profile (Hillier et al. 1998; their Fig. 3), and it is nearly a spectroscopic twin to η Car (Hillier et al. 2001).

In total, there are more than a dozen absorption components to the Na I D complex in our data. The extreme blue portion of the complex blends with He I $\lambda 5876$, and we observe variability in both the stellar and intervening components of the complex. First, in the Na I D₁ line (Fig. Set 1.12), we see a narrow absorption component at $\approx -145 \text{ km s}^{-1}$ that strengthens near phase 0.0 (\sim HJD 2,454,840). In Paper 1, we saw a similar component in H α at -144 km s^{-1} that appeared just prior to phase 0.0, which is attributed to gas in the Little Homunculus. We postulated that when the hot secondary goes behind the wind of the primary in our line of sight, that the intervening gas from the Little Homunculus drops in ionization due to quenching of Lyman continuum from the secondary star by the enveloping primary wind. As the gas cools, more Na I is in the ground state, allowing for a larger absorption in this resonance line. Secondly, the dynamical spectra show that just after phase 0, the deep absorption components at $\sim -500 \text{ km s}^{-1}$ for both Na I lines seem to become wider and deeper. This is similar to the changes seen with H α and Fe II, although the ionization energies are very different.

3.5. Si II Profiles

The Si II $\lambda 6371$ line is blended with Fe II lines at 6371 and 6373 Å and is best analyzed as a complex rather than individual lines. However, the Si II $\lambda 6347$ transition is mostly isolated from other lines (Fig. Set 1.13). The Si II lines show a radial velocity movement towards longer wavelengths near phase 0.0, as well as a development of a P Cygni absorption that begins near phase 0.0. Multiple narrow emission lines from the Weigelt knots are present, and these weaken or disappear during the event. The behavior of this profile is reminiscent of that of the He I lines discussed previously.

3.6. Fe II Profiles

Many Fe II lines are present in the optical spectrum of η Car. We examined the lines at 5169, 5197, 5234, 5316, 6238, 6248, and 6456 Å. The dynamical spectra and line plots for these transitions are shown in Fig. Set 1.15–1.21 respectively. Other Fe II lines were either blended with nearby transitions or had too low a signal to study their variations. The strongest of these transitions (Fe II $\lambda 5169$, 5234, and 6456) developed P Cygni profiles during the event, and these lines qualitatively show an increase in P Cygni absorption and small increases in emission line strength between the P Cygni absorption trough and Weigelt knot emission. The timing of the P Cygni absorption development happens slightly later for these transitions (between HJD 2,454,842–2,454,852) than for the Balmer lines ($\sim 2,454,837$ –2,454,840) and the He I lines (HJD 2,454,838) discussed previously.

4. Wind Line Measurements

4.1. Equivalent Widths

We measured the equivalent widths of ten optical wind lines during the time of the photometric minimum, and these are listed in column 4 of Table 2. These lines were selected based upon transitions that were relatively isolated with relatively little contamination from blends. Because the profiles have complicated shapes in general, we simply performed a numerical integration across the entire blue absorption trough and red emission peak using the integration limits listed in columns 6 and 7 of Table 1. The net equivalent widths have typical uncertainties of ± 0.5 Å or larger in strong lines. The somewhat arbitrary method of rectifying the spectra means that there may be systematic differences with measurements made by other investigators, but relative variations in our measurements are reliable. As none

of these transitions have the remarkable strength of $H\alpha$ and often have P Cygni absorption at nearly the same strength as the emission, we did not correct these equivalent widths for a changing continuum flux as we did for $H\alpha$ measurements in Paper 1.

We show in Figure 2 the time evolution of the equivalent widths for these optical lines and $H\alpha$ (Paper 1). The largest relative changes occurred in the He I and Si II lines (and probably also in the N II lines that were too weak to measure securely). All these lines experienced a drop in emission strength near phase 0.0 due the emergence of an absorption component and a decrease in the emission peak. A similar decrease occurred in the $H\alpha$ emission strength but with a lower fractional change. The variations in the Fe II emission strength were all small, due in part to a near balance between increases in both the absorption trough and emission peak strength. Note that we do not include in Figure 2 our results for He I $\lambda\lambda 4922, 5016$ because these features are significantly blended with Fe II lines (Zethson et al. 2012).

4.2. P Cygni Absorption Velocities

We measured a radial velocity for the P Cygni absorption components by determining the minimum flux position as we did for the $H\alpha$ transition of P Cygni in Richardson et al. (2011). This velocity V_{\min} was set by finding the zero crossing in the numerical derivative of a smoothed version of the spectral lines. The S/N ratio was generally sufficient to determine V_{\min} reliably in those cases where the P Cygni absorption was present. We estimate the uncertainty as approximately $\pm 5 \text{ km s}^{-1}$ based upon the night-to-night scatter after removal of the velocity trends.

We measured V_{\min} for 14 transitions, and these measurements are listed in column 5 of Table 2. The temporal variations of V_{\min} are shown in Figure 3 in panels for each line species. We caution again that the results for He I $\lambda\lambda 4922, 5015$ are significantly affected by blends with Fe II lines. The largest variations occurred in the He I, N II, and Si II lines, all of which showed a systematic red-ward shift of $\approx 200 \text{ km s}^{-1}$ after phase 0.0. Inspection of the actual profiles in Figure Set 1 suggests that this velocity shift is caused by a systematic reduction in absorption strength with time that starts at the most extreme negative velocities and progresses towards zero velocity. Thus, these changes might be better regarded as representative of an absorption component that becomes narrower over time, rather than a wholesale shift of a fixed-width absorption feature. The measured changes in the other lines with absorption components are generally small, consistent with their constant appearance in Figure Set 1.

4.3. Emission Bisector Velocities

In Paper 1, we presented emission line bisector velocities for $H\alpha$ across the 2009 spectroscopic event in order to search for evidence of spatial asymmetries in the emitting volume. Here we present emission line bisector velocities for He I and several other lines with well-defined emission peaks. These were measured by estimating a bisector velocity V_b at $\sim 20\%$ of the peak height above the continuum. The results appear in column 6 of Table 2. We estimate that the uncertainties are generally $\pm 5 \text{ km s}^{-1}$ for the most reliable cases based upon the scatter around the de-trended curves. However, many of these lines are fairly weak, so the measurement is complicated by the low contrast between the emission line and continuum and by blending with components from the Weigelt knots or other emission lines. Therefore, we only present in Figure 4 measurements of V_b for those cases with clearly defined emission peaks. The largest changes occurred in the He I $\lambda\lambda 6678, 7065$ and Si II $\lambda 6347$ lines. All these lines show an increase in velocity of $\approx 200 \text{ km s}^{-1}$ that begins around phase 0.0. Curiously there was also a local flattening in the velocity curves of these lines around phase 0.005 that is suggestive of some structure in the wind geometry. The emission bisector velocities of $H\alpha$ and Fe II $\lambda 5316$ show similar trends but with much smaller amplitude.

5. Illuminated Hemisphere Model for He I

The wind line variations documented above reflect how the hot secondary alters the wind properties as the companion plunges deep into the envelope of the primary. We can begin to understand the wind and line variations by considering the large amplitude changes observed in the He I lines. The He I lines probe the inner part of the stellar wind. The ionization energy needed for a recombination line such as He I $\lambda 6678$ is 24 eV, and the models of Hillier et al. (2001) show that these lines should form at a radius of $\sim 11R_*$ (3 AU) from the primary. Madura et al. (2012) estimate that the binary semi-major axis is 15.4 AU and the eccentricity is 0.9, so that the periastron separation is only 1.5 AU, similar to or smaller than the He I line forming region. This implies that the He I lines should form near the region of a wind-wind collision zone at periastron, and this expectation is borne out in detailed models of the wind ionization zones (Clementel et al. 2015b).

The main orbital-phase related variations of the He I lines are probably linked to changing illumination of the primary star by the flux from the companion and the wind-wind collision region between the stars. We show in Figure 5 the orientation of the orbit of the secondary relative to the primary as projected onto the sky. The orbital elements are from Madura et al. (2012): $a = 15.4 \text{ AU}$, $d = 2.3 \text{ kpc}$, $e = 0.9$, $i = 138^\circ$, $\omega_p = 263^\circ$ (longitude of periastron for the primary), and $\Omega = \text{PA}_z - 90^\circ = 227^\circ$ (longitude of the ascending node).

The top four panels show the position of the secondary (marked by a plus sign) at four orbital phases (arranged in clockwise order like the sense of the orbit in the sky). The open circle at the bottom left represents the primary star, and the brighter portion of the disk shows the hemisphere facing the secondary (mostly hidden behind the primary at phase 0.0).

If emission lines like He I $\lambda 6678$ form in the illuminated hemisphere of the primary wind, then we expect that the emission would be stronger (weaker) when that hemisphere is orientated towards (away) from us. Let us assume for simplicity that the emission flux varies with the projected area of the illuminated region. Then the fraction of the projected disk illuminated by the secondary is given by

$$F = \frac{1}{2}(1 + \cos a)$$

where a is the angle from the observer through the primary to the secondary. This angle depends on the orbital geometry as

$$\cos a = -\sin(\nu + \omega_s) \sin i$$

where ν is the time dependent true anomaly, ω_s is the longitude of periastron for the secondary star ($\omega_s = \omega_p + 180^\circ$), and i is the inclination.

We compare the orbital variation of the illuminated fraction with the the equivalent width measurements of He I $\lambda 6678$ in Figure 6 (left). A single linear scaling parameter was selected to match the amplitudes of both quantities. We assumed that periastron occurs at phase 0.0, and we adopted an eccentricity $e = 0.9$ and three trial values of longitude of periastron, $\omega_p = 200^\circ$ (solid line), $\omega_p = 240^\circ$ (dashed line), and $\omega_p = 263^\circ$ (dotted line). The latter estimate of $\omega_p = 263^\circ$ was derived from the analysis of Madura et al. (2012) from their analysis of the forbidden line emission resolved by HST/STIS, with $\omega_p = 240^\circ$ derived from an analysis of the He II $\lambda 4686$ variability by M. Teodoro et al. (2015, in preparation). This model does fit the time and approximate duration of the emission weakening observed around periastron which occurs when the companion is almost behind the primary (assuming a longitude of periastron for the primary of $\omega_p = 263^\circ$, which is close to the value for periastron at conjunction, $\omega_p = 270^\circ$). However, that model suggests that the drop is more or less symmetrical around periastron, while the observations suggest a slower recovery. A better match is made with a smaller longitude of periastron, $\omega_p = 240^\circ$ (dashed line). The overall good match of this simple model with the observed emission variations around periastron suggests that the emission is localized in the hemisphere facing the companion. We note that this illumination would arise from a combination of both the incident flux of the secondary star and the apex of the wind-wind collision zone. The deviation between the model and the observations at later time (near phase 12.2) may be due to the presence of strong P Cygni absorption at these epochs that causes a decrease in emission line flux.

The illuminated hemisphere model can also address the issue of the radial velocity changes observed around periastron. If the emission lines form predominantly in the wind of the primary that is facing the companion, then we would expect to see outflow directed away from the illuminated hemisphere and towards the companion, and at periastron the wind flow would be directed away from us. We calculated the mean radial velocity by adopting a constant radial wind outflow of $v_\infty = 500 \text{ km s}^{-1}$ (assuming the wind has reached terminal speed in the line forming region). The observed mean Doppler shift over the illuminated hemisphere is then given by

$$v_r = -v_\infty \int \cos \theta dA / \int dA$$

where θ is the angle (in radians) from the stellar surface normal to the observer and the area integral is taken over the illuminated region of the disk. The analytical solution of the integral is

$$v_r = v_\infty \frac{4}{3\pi} \frac{\pi + \cos a \sin a - a}{1 + \cos a}$$

where again a is the angle from the observer through the primary to the secondary (with a time dependence as given above).

The predicted wind velocity as a function of orbital phase is shown in Figure 6 (right) and is compared to the measured line bisector velocities for He I $\lambda 6678$. Here we applied a single constant offset velocity to match the predictions with the observed radial velocities. This constant was taken as the difference between the mid-range velocity of the bisector measurements (for the red-shifted position of the emission peak) and the mid-range velocity of the model. We also included the relatively small orbital motion of η Car A with the mean wind velocity. The nominal model with $\omega_p = 263^\circ$ (dotted line) shows the right amplitude, but it appears more symmetrical than the observations that show a more extended decline. A model with a smaller longitude of periastron, $\omega_p = 240^\circ$ (dashed line), does a better job of matching the observations. The agreement is suggestive that the simple model is on the right track. The differences at later time may again be related to the increased P Cygni absorption that causes a red-ward (positive) shift in the bisector velocity.

We emphasize that this model is purely geometric and does not account for physical processes that must be important. For example, we have neglected the change in separation with orbital phase that is clearly related to the flux from the secondary incident on the primary star, and we ignored radiative transfer issues related to heating of the primary's wind and photosphere. More fundamentally, we have treated the secondary as a point source, whereas in fact it is a hot star with a fast wind that comes so close to the primary at periastron that the wind interaction zone reaches close to where the He I line formation zone occurs. The location and structure of the zones of singly-ionized He in the wind of

η Car A have recently been investigated in numerical models by Clementel et al. (2015a,b). In particular, Clementel et al. (2015b) have calculated the He ionization structure near periastron, and they find potential emission zones in the inner wind of A, the pre-shock wind of A near the apex of the wind-wind collision zone, and in post-shock wind gas that is also photoionized by B. The combination of emission from all these zones might indeed cause an asymmetry in the wind emission in the sense of enhanced emission in the direction of companion. Consequently, our illuminated hemisphere model might be regarded as a first order approximation of a highly structured wind and interaction region.

6. Conclusions

The data shown in Figure Set 1 present a detailed account of the optical spectral variability of the system during the 2009 event, with the best timing cadence of any previous campaign. These data portray how the wind lines of the primary are influenced by the close proximity of the hot companion at periastron. The line variations are different in the transitions of ions that form preferentially at different heights in the expanding atmosphere of the primary star. We found that all the lines display the emergence of a blue-shifted, absorption trough near or shortly after phase 0.0 (near periastron). The absorption component lasts only 10 days or so in some ions (He I, N II) but remains throughout the event in others (H α , H β). We measured the net combined equivalent width of the blue absorption trough and red emission peak (plus other blends in some cases) for the selected lines, and in most cases we find that the equivalent width dropped around periastron due to the combined effects of increased blue absorption and decreased emission. The largest relative changes occurred in the lines of He I and Si II (and probably N II but these lines are difficult to measure). Some of the lines displayed Doppler shift changes that we measured in two ways. First, we determined the minimum flux position V_{\min} in the absorption trough whenever possible. This absorption velocity is relatively constant in the H and Fe II lines, but it increases with time in the lines of He I, N II, and Si II as the absorption progressively disappears at the lower, more extreme Doppler shifts. Second, we derived a bisector velocity V_b that measures the Doppler shift of the red emission peak, and these show a large change of $\approx +200$ km s $^{-1}$ during the event for the lines of He I and Si II. On the other hand, changes in the H and Fe II lines were quite small.

All these variations are probably related to changes in the ionization state of the wind gas caused by the close proximity of the hot companion star around periastron. The orbit of the companion has yet to be directly measured, but the changes in the illumination of the hot circumstellar gas by the companion can set important constraints on the orbital

elements. The documented illumination changes for the spectral lines in this data set can successfully rule out the family of orbital elements that have the companion star between the observer and the primary at periastron. Madura et al. (2012) developed a three-dimensional model for the circumstellar gas that they fit to angularly resolved spectroscopic observations from HST/STIS, and their work indicates that periastron occurs near companion superior conjunction. Thus, we expect that the portion of the wind illuminated by the hot companion will change quickly around periastron, and the hemisphere facing the companion at periastron will be directed away from us. The idea that the hemisphere facing the companion will be most influenced by its ionizing flux was the basis for our simple model (§5) for the variations in the He I $\lambda 6678$ line. The model shows that for reasonable values of the longitude of periastron of the primary ω_p we can approximately explain the decline and recovery of the emission equivalent width as the result of the changing orientation of the emitting hemisphere that faces the companion. Likewise, the model accounts for the red-ward Doppler shift of the emission as the result of the changing orientation away from us of the radial outflow in the illuminated hemisphere of the primary star. The reality of He I line formation is complicated by heating in the wind-wind collision zone (Clementel et al. 2015b), but we suspect that any large scale asymmetry related to an emitting gas distribution in the vicinity of the hemisphere of the primary facing the secondary will create line strength and Doppler shift variations similar to those predicted by the simple model.

The success of our illuminated hemisphere model and the three-dimensional colliding winds model of Madura et al. (2012) in explaining the spectral variations that occur around periastron results from our adoption of a longitude of periastron that places the companion beyond the primary at the time of periastron. The observed equivalent width and radial velocity variations of the wind lines can only be matched if the illuminated hemisphere of the primary is partially directed away from us at periastron towards a more distant companion. Thus, earlier suggestions that companion is in the foreground at periastron (Kashi et al. 2011) are no longer tenable.

The differences in the amplitudes of the emission strength and Doppler shift variations among the various line species probably result from differences in the radius of line formation. Hillier et al. (2001) present calculations of the distribution of the line emission contributions as a function of distance from the center of the primary (see their Figs. 15 and 16), and they find that lines like H α and Fe II $\lambda 4923$ form relatively far out in the wind (at $\log(r/R_\star) = 1.7$ and 2.2, respectively), while other, higher excitation lines like He I $\lambda 5876$ form closer to the star (at $\log(r/R_\star) = 0.6$). Based upon the ionization and excitation energies (Table 1), we expect that the N II lines form in a similar location to the He I lines, while the Si II lines originate at a larger radius intermediate between those of He I and H α . Thus, the similarities in the spectral variations of the He I and N II lines probably result from their formation in

a similar location (and likewise for the $H\alpha$ and Fe II lines). The fact that the wind line variations are much smaller for lines formed far out in the wind ($H\alpha$ and Fe II) probably indicates that the photoionization of the wind by the companion is quite localized around periastron. The companion attains such a small periastron separation ($\log(d/R_\star) = 0.6$) that it must be deeply immersed in the wind of the primary then. We suspect that the ionizing photons from the companion only penetrate a small distance in the envelope of the primary, so that conditions in the outer parts of the wind (where the lower excitation lines form) see relatively little change in ionization state, leading to relatively small variations in the H and Fe II lines.

The primary of η Car acts as an occulting disk to the flux of the hot companion, so gas in the shadow cone on the side of primary facing away from the companion may experience conditions of a stellar wind undisturbed by the companion (Richardson et al. 2010; Groh et al. 2012). This part of the undisturbed wind will appear projected against the photosphere of the primary around periastron when the companion is beyond the plane of the sky. We suggest that the appearance of the P Cygni absorption components near periastron is the result of our line of sight crossing through the undisturbed wind then. With the decline in photoionizing flux in this region, the atomic populations may favor absorption or scattering of photons from the primary that are directed toward us. The shorter duration of the absorption component phase in the He I and N II lines is probably due to the close proximity of the hot companion and line forming region as the companion reappears above the optically thick horizon of the primary as seen by the wind gas along our line of sight to the primary. On the other hand, the longer duration of the absorption phase in $H\alpha$ may be due to the longer path length of the ray from the primary along our line of sight and to the longer timescale for the wind opacity decline that would allow the photoionizing flux of the companion to reach large distances out into the wind of the primary.

The suggestion that the presence of an absorption trough in $H\alpha$ represents our temporary sampling of the undisturbed wind of η Car A is supported by angularly resolved spectroscopy of light scattered by dust in the Homunculus nebula. For example, Mehner et al. (2011a) show how the $H\delta$ line presents a P Cygni-type absorption at most orbital phases at an offset position that scatters light from the polar direction of the primary. If this polar wind is relatively unaffected by the changing photoionization of the companion, then perhaps primary’s wind only suffers significant ionization changes in sectors centered on the orbital plane. The similarity in the appearance of $H\delta$ in the star’s spectrum just after periastron with that for the polar wind (see Fig. 7 of Mehner et al. 2011a) suggests that our line of sight to the primary traverses comparable wind properties at that time. Thus, the particular orientation of the companion lying beyond the primary at periastron probably allows us to view the primary’s wind for a short while then without the ionization changes

imposed by the secondary’s flux.

Our program to monitor η Car with the CTIO 1.5m telescope and fiber fed echelle spectrograph was very successful in documenting the spectral changes through the 2009 event. We have continued this monitoring program through to the 2014 periastron passage and beyond. In future work we plan to make a detailed comparison of the wind line variations between these two events in order to investigate the issue of long-term variations in the mass loss rate (Mehner et al. 2012) and to confront the predictions of hydrodynamical models and radiative transfer calculations for the ionization zones created by colliding winds (Clementel et al. 2015b).

These spectra were collected with the CTIO 1.5 m telescope, which is operated by the SMARTS Consortium. We thank Todd Henry for his assistance in obtaining the spectra during the spectroscopic event. We are extremely grateful to Fred Walter (Stony Brook University) for his careful scheduling of this program and to the CTIO SMARTS staff for queue observing support. The spectra analyzed in the post-event state were obtained with NOAO programs 09b-153, 12a-0216, and 12b-0194. This research has made use of the data archive for the HST Treasury Program on Eta Carinae (GO 9973) which is available on-line at <http://etacar.umn.edu>. The archive is supported by the University of Minnesota and the Space Telescope Science Institute under contract with NASA. NDR gratefully acknowledges his CRAQ fellowship. This work was supported by the National Science Foundation under grants AST-1009080 and AST-1411654. AFJM is grateful for support from NSERC (Canada) and FQRNT (Quebec). Institutional support has been provided from the GSU College of Arts and Sciences and from the Research Program Enhancement Fund of the Board of Regents of the University System of Georgia, administered through the GSU Office of the Vice President for Research and Economic Development.

REFERENCES

- Barden, S. C., & Ingerson, T. E. 1998, in *Fiber Optics in Astronomy III* (ASP Conf. Ser., Vol. 152), ed. S. Arribas, E. Mediavilla, & F. Watson (San Francisco: ASP), 60
- Clementel, N., Madura, T. I., Kruip, C. J. H., & Paardekooper, J.-P. 2015b, *MNRAS*, 450, 1388
- Clementel, N., Madura, T. I., Kruip, C. J. H., Paardekooper, J.-P., & Gull, T. R. 2015a, *MNRAS*, 447, 2445
- Corcoran, M. F. 2005, *AJ*, 129, 2018

- Corcoran, M. F., Hamaguchi, K., Pittard, J. M., et al., 2010, *ApJ*, 725, 1528
- Damineli, A., Conti, P. S., & Lopes, D. F. 1997, *NewA*, 2, 107
- Damineli, A., Hillier, D. J., Corcoran, M. F., et al. 2008a, *MNRAS*, 384, 1649
- Damineli, A., Hillier, D. J., Corcoran, M. F., et al. 2008b, *MNRAS*, 386, 2330
- Damineli, A., Kaufer, A., Wolf, B., et al. 2000, *ApJ*, 528, L101
- Davidson, K., & Humphreys, R. M. 1997, *ARA&A*, 35, 1
- Fernández-Lajús, E., Fariña, C., Calderón, J. P., et al. 2010, *NewA*, 15, 108
- Fernández Lajús, E., Gamen, R., Schwartz, M., et al. 2003, *IBVS*, 5477, 1
- Gaviola, E. 1953, *ApJ*, 118, 234
- Groh, J. H., Hillier, D. J., Madura, T. I., & Weigelt, G. 2012, *MNRAS*, 423, 1623
- Gull, T. R., Kober, G., Vieira Kober, G., & Nielsen, K. 2006, *ApJS*, 163, 173
- Gull, T. R., Madura, T. I., Groh, J. H., & Corcoran, M. F. 2011, *ApJ*, 743, 3L
- Gull, T. R., Nielsen, K., Corcoran, M. F., et al. 2009, *MNRAS*, 396, 1308
- Gull, T. R., Vieira, G., Bruhweiler, F., et al. 2005, *ApJ*, 620, 442
- Hillier, D. J., Crowther, P. A., Najarro, F., & Fullerton, A. W. 1998, *A&A*, 340, 483
- Hillier, D. J., Davidson, K., Ishibashi, K., & Gull, T. 2001, *ApJ*, 553, 837
- Ishibashi, K., Gull, T. R., Davidson, K., et al. 2003, *AJ*, 125, 3222
- Kashi, A., Soker, N., & Akashi, M. 2011, *MNRAS*, 413, 2658
- Madura, T., Gull, T. R., Owocki, S. P., et al., 2012, *MNRAS*, 420, 2064
- Mehner, A., Davidson, K., & Ferland, G. J. 2011b, *ApJ*, 737, 70
- Mehner, A., Davidson, K., Martin, J. C., et al. 2011a, *ApJ*, 740, 80
- Nielsen, K. E., Corcoran, M. F., Gull, T. R., et al. 2007, *ApJ*, 660, 669
- Nielsen, K. E., Vieira Kober, G., Weis, K., et al. 2009, *ApJS*, 181, 473

- Okazaki, A. T., Owocki, S. P., Russell, C. M. P., & Corcoran, M. F. 2008, MNRAS, 388, L39
- Parkin, E. R., Pittard, J. M., Corcoran, M. F., Hamaguchi, K., & Stevens, I. R. 2009, MNRAS, 394, 1758
- Richardson, N. D., Gies, D. R., Henry, T. J., Fernández-Lajús, E., & Okazaki, A. T. 2010, AJ, 139, 1534 (Paper 1)
- Richardson, N. D., Morrison, N. D., Gies, D. R., et al. 2011, AJ, 141, 120
- Smith, N. 2006, ApJ, 644, 1151
- Teodoro, M., Daminieli, A., Arias, J., et al. 2012, ApJ, 746, 73
- Tokovinin, A., Fischer, D., Bonati, M., et al. 2013, PASP, 125, 1336
- van Genderen, A. M., Sterken, C., & Allen, W. H. 2003, A&A, 405, 1057
- Weigelt, G., & Ebersberger, J. 1986, A&A, 163, L5
- Whitelock, P. A., Feast, M. W., Marang, F., & Breedt, E. 2004, MNRAS, 352, 447
- Zethson, T., Johansson, S., Hartman, H., & Gull, T. R. 2012, A&A, 540, 133

Fig. Set 1. Observed line profiles during η Car's 2009 event

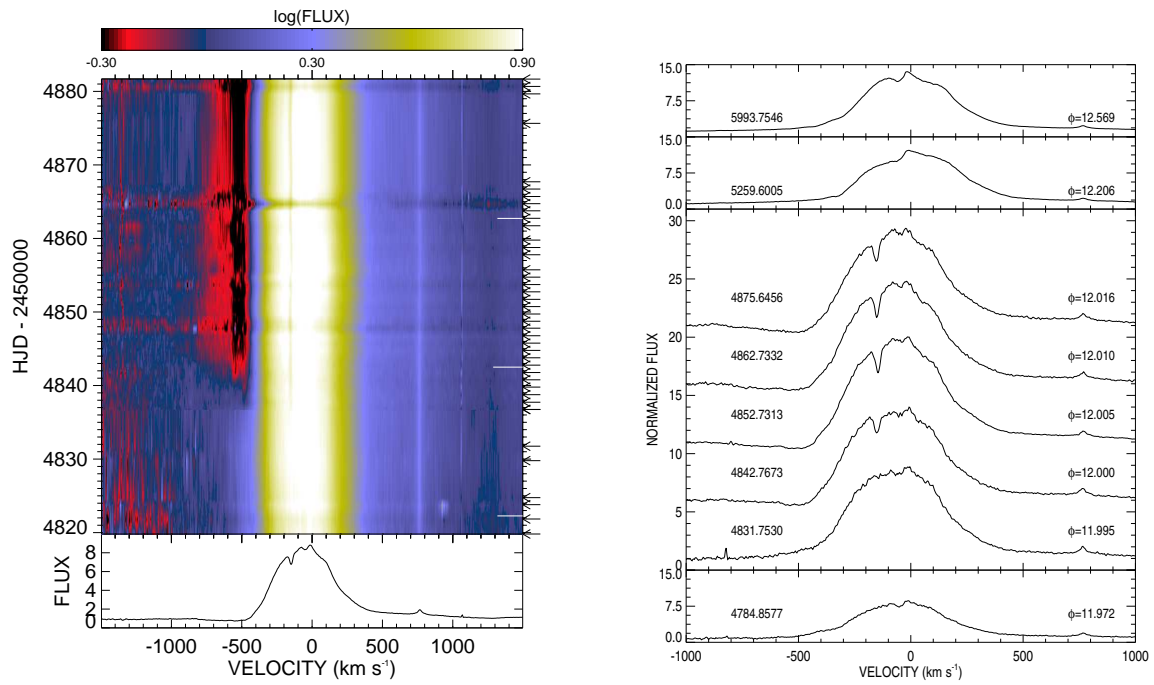


Fig. 1.1.— Dynamical (left) and line plots (right) of H β during the 2009 event. The white horizontal bars on the dynamical representation indicate phases 11.99, 12.00, and 12.01.

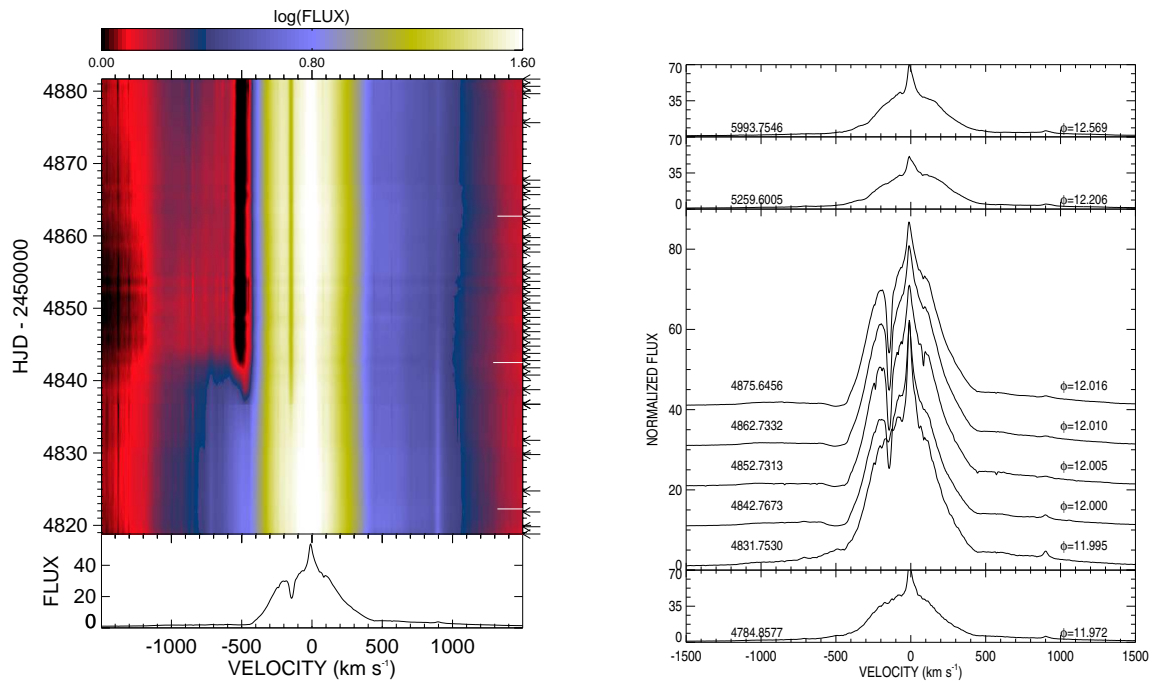


Fig. 1.2.— Dynamical (left) and line plots (right) of H α during the 2009 event. The white horizontal bars on the dynamical representation indicate phases 11.99, 12.00, and 12.01.

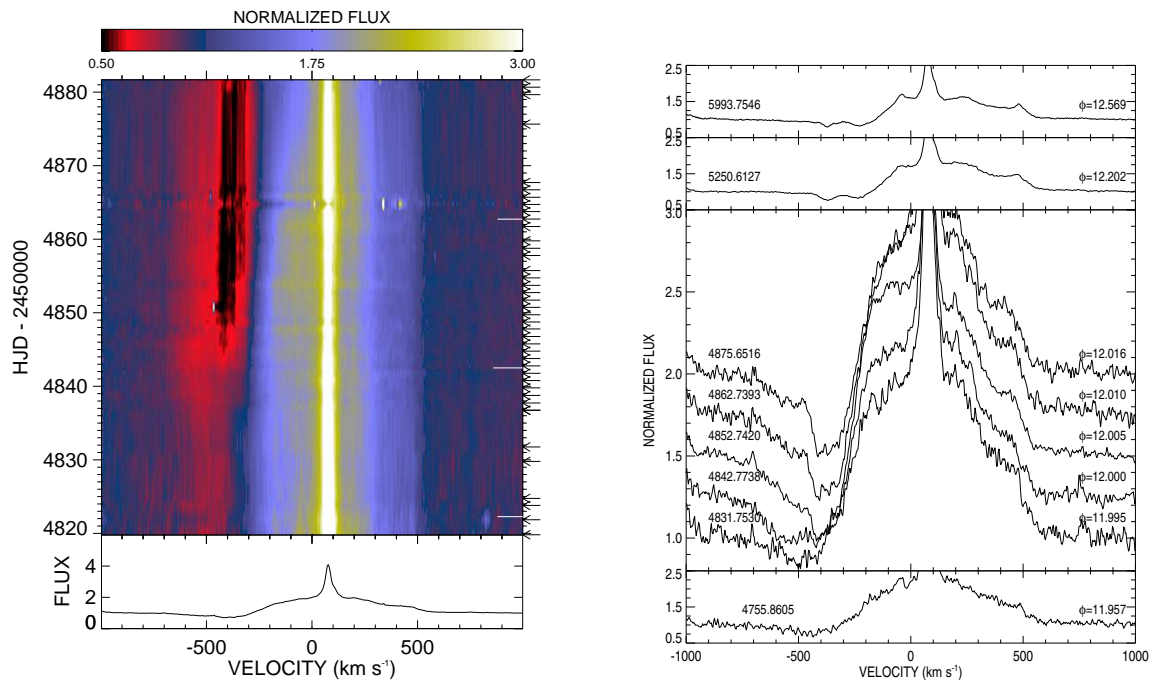


Fig. 1.3.— Dynamical (left) and line plots (right) of He I $\lambda 4922$ during the 2009 event. The white horizontal bars on the dynamical representation indicate phases 11.99, 12.00, and 12.01.

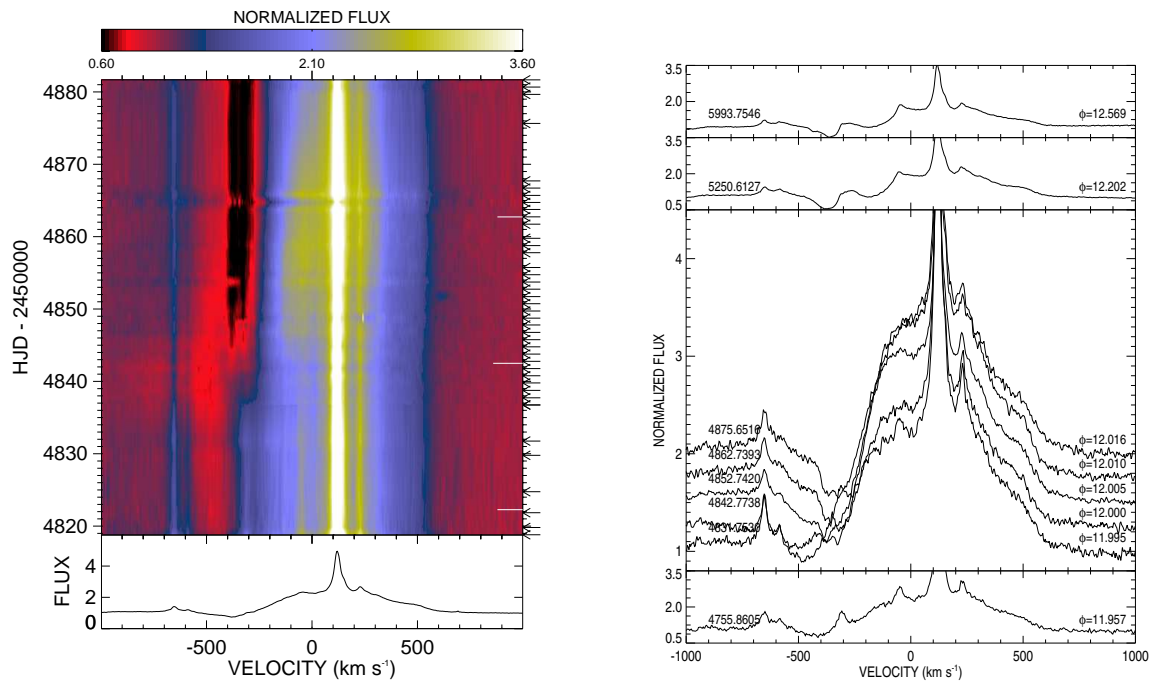


Fig. 1.4.— Dynamical (left) and line plots (right) of He I $\lambda 5015$ during the 2009 event. The white horizontal bars on the dynamical representation indicate phases 11.99, 12.00, and 12.01.

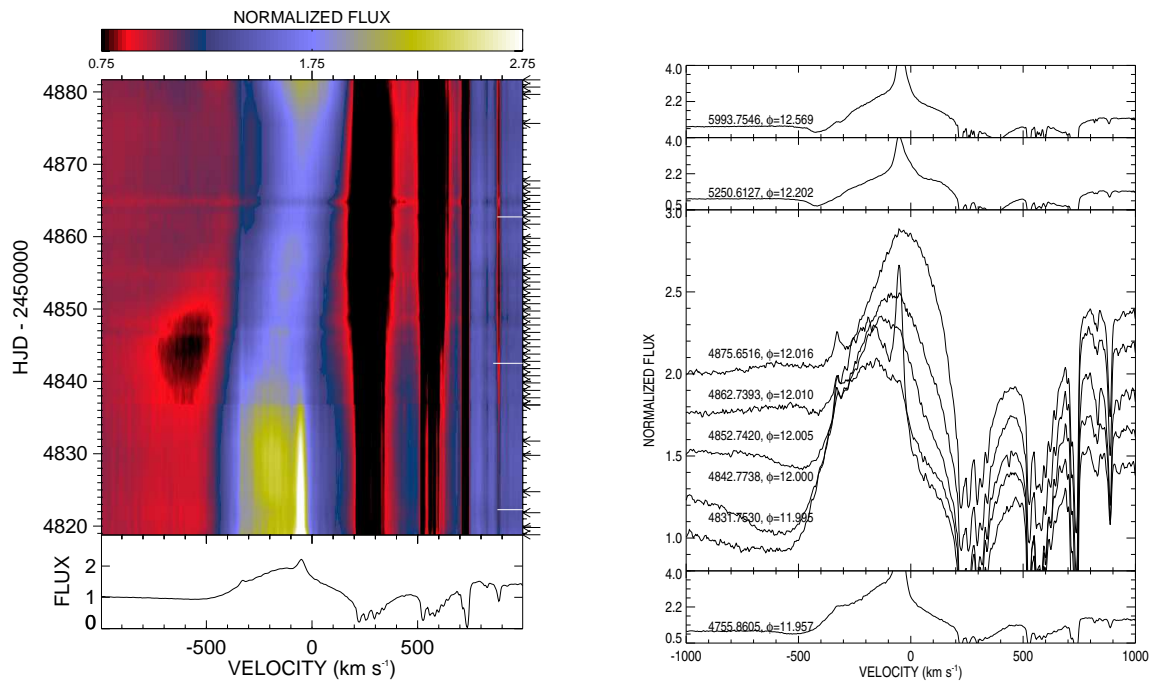


Fig. 1.5.— Dynamical (left) and line plots (right) of He I $\lambda 5876$ during the 2009 event. The white horizontal bars on the dynamical representation indicate phases 11.99, 12.00, and 12.01.

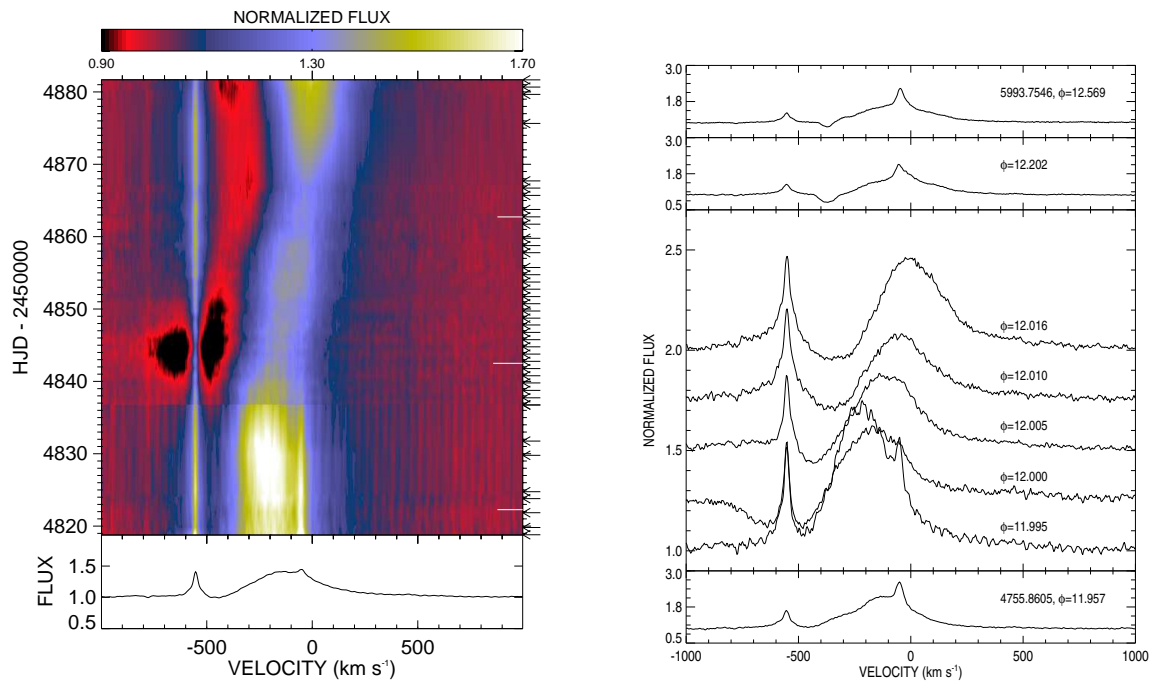


Fig. 1.6.— Dynamical (left) and line plots (right) of He I $\lambda 6678$ during the 2009 event. The white horizontal bars on the dynamical representation indicate phases 11.99, 12.00, and 12.01.

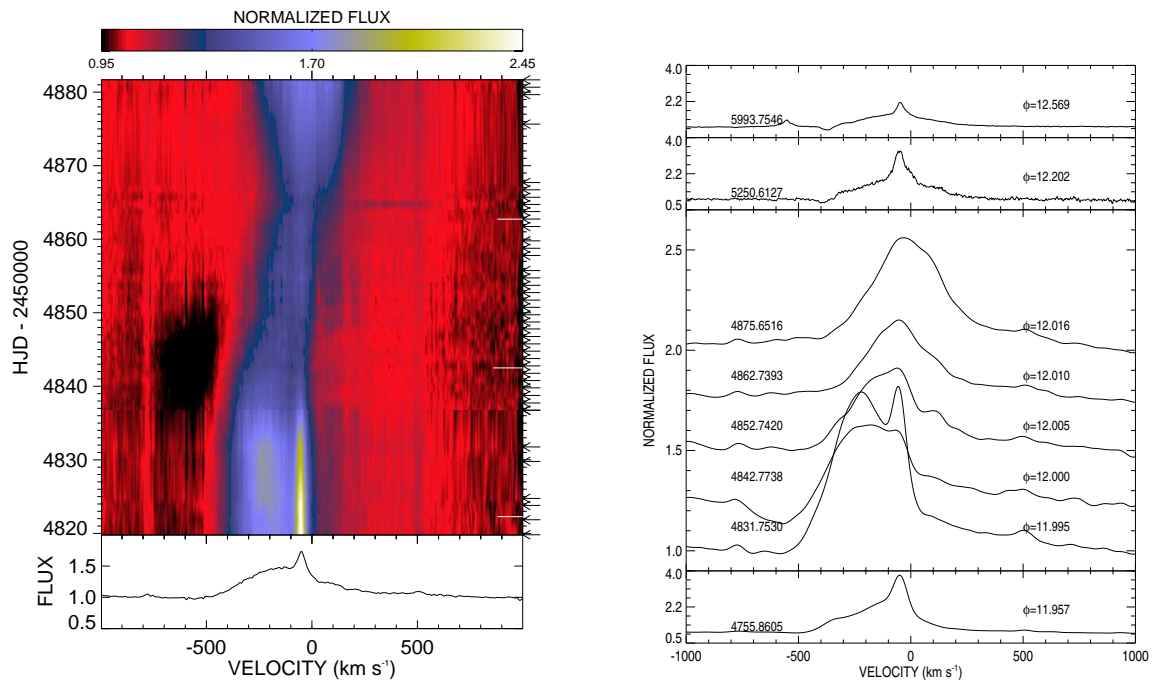


Fig. 1.7.— Dynamical (left) and line plots (right) of He I $\lambda 7065$ during the 2009 event. The white horizontal bars on the dynamical representation indicate phases 11.99, 12.00, and 12.01.

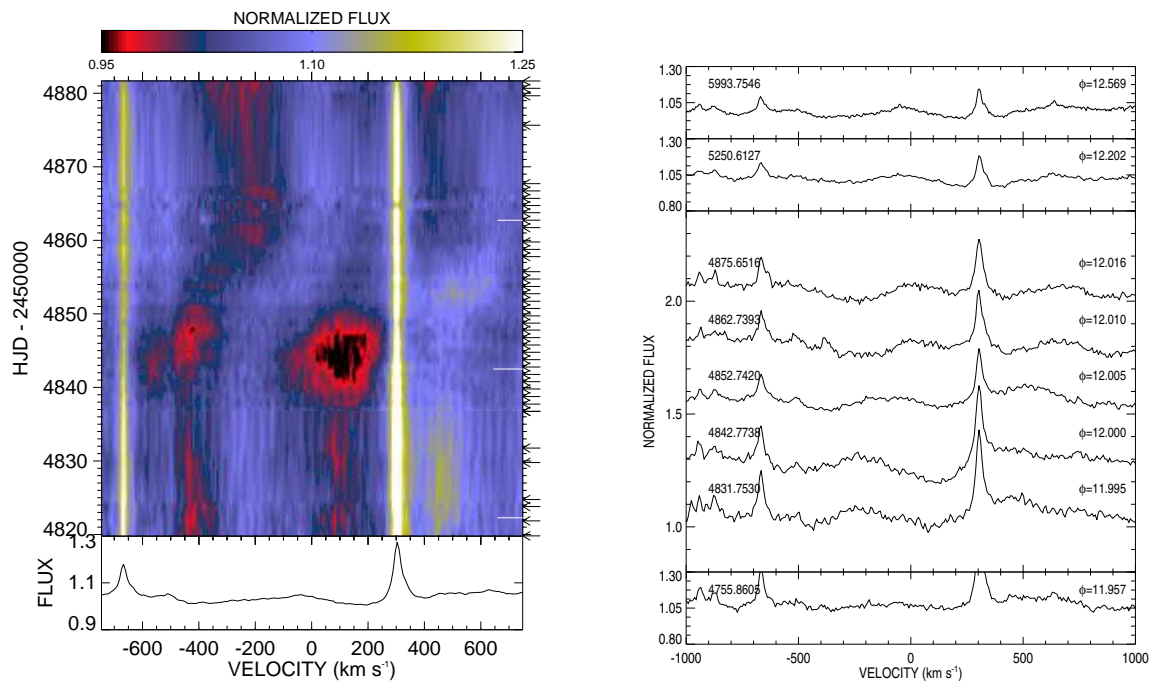


Fig. 1.8.— Dynamical (left) and line plots (right) of N II $\lambda 5666$ during the 2009 event. The white horizontal bars on the dynamical representation indicate phases 11.99, 12.00, and 12.01. Note that N II $\lambda 5676$ is visible on the right.

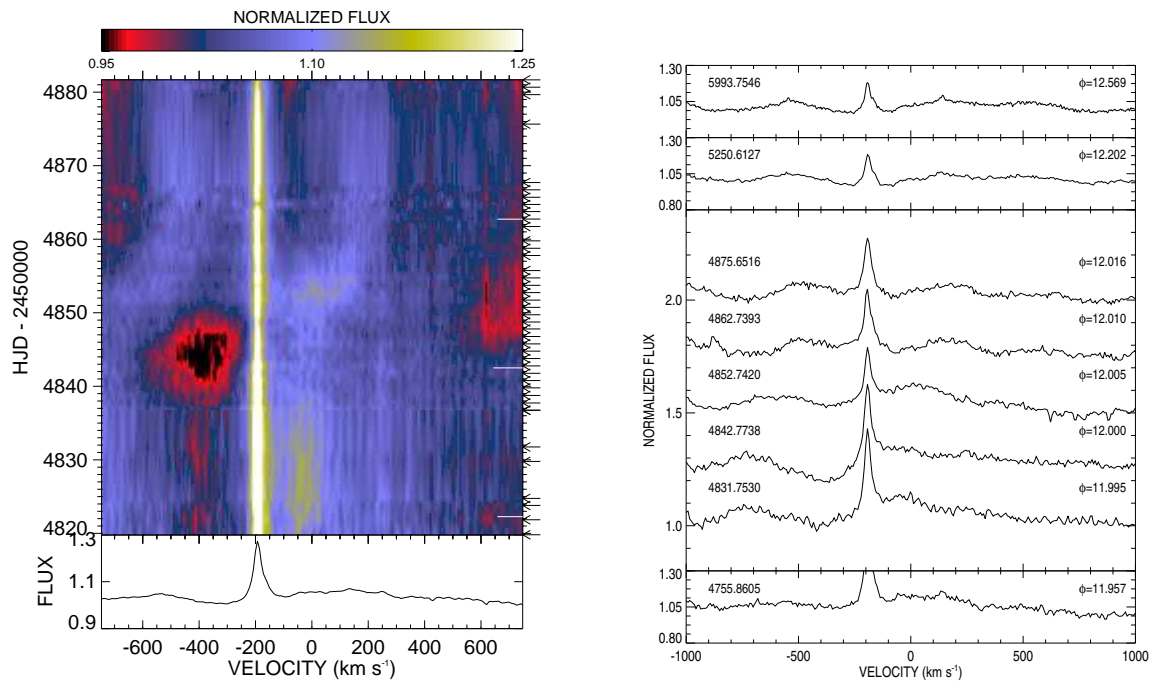


Fig. 1.9.— Dynamical (left) and line plots (right) of N II $\lambda 5676$ during the 2009 event. The white horizontal bars on the dynamical representation indicate phases 11.99, 12.00, and 12.01.

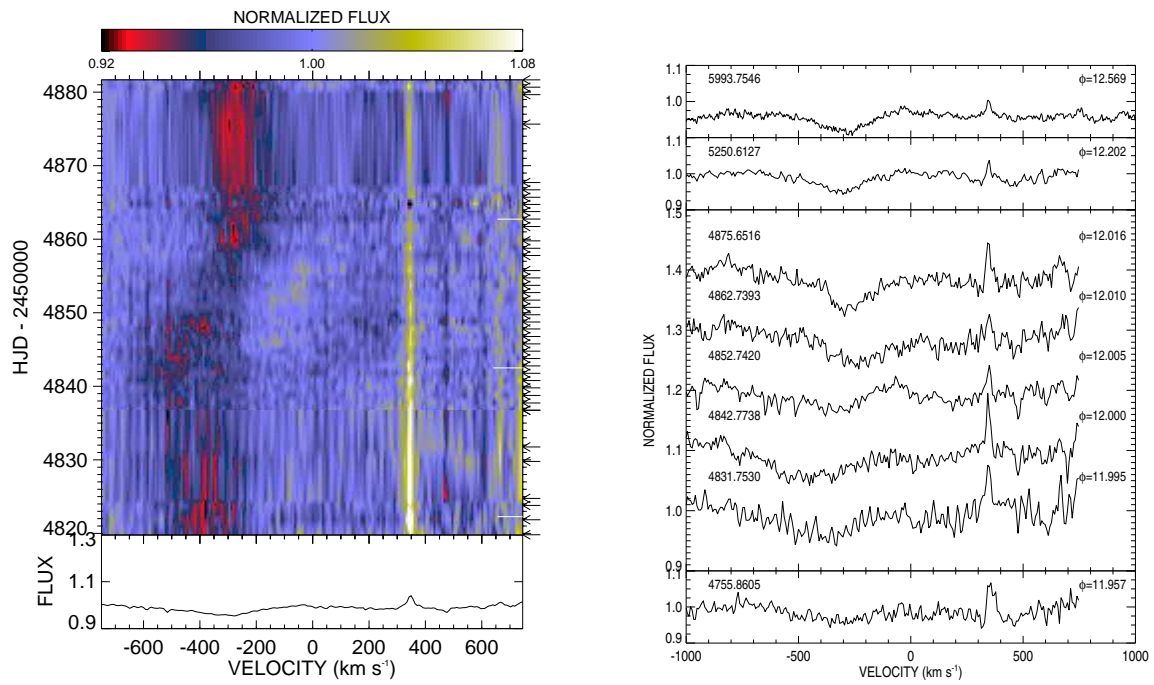


Fig. 1.10.— Dynamical (left) and line plots (right) of N II $\lambda 5711$ during the 2009 event. The white horizontal bars on the dynamical representation indicate phases 11.99, 12.00, and 12.01.

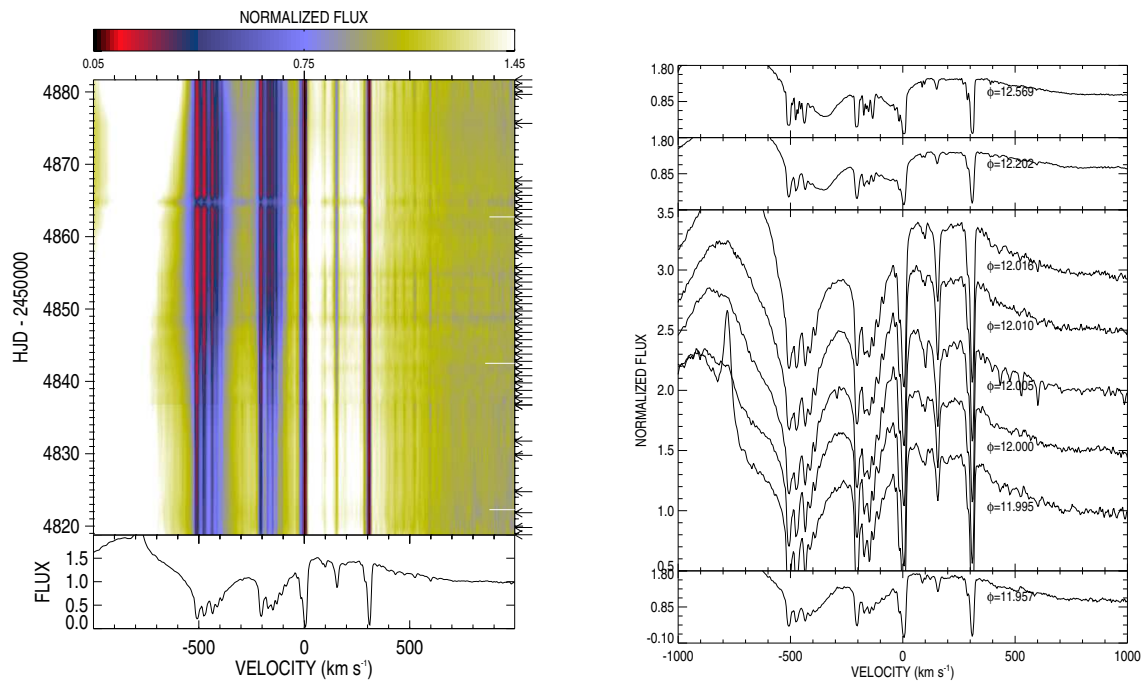


Fig. 1.11.— Dynamical (left) and line plots (right) of Na I D₂λ5890 during the 2009 event. The white horizontal bars on the dynamical representation indicate phases 11.99, 12.00, and 12.01.

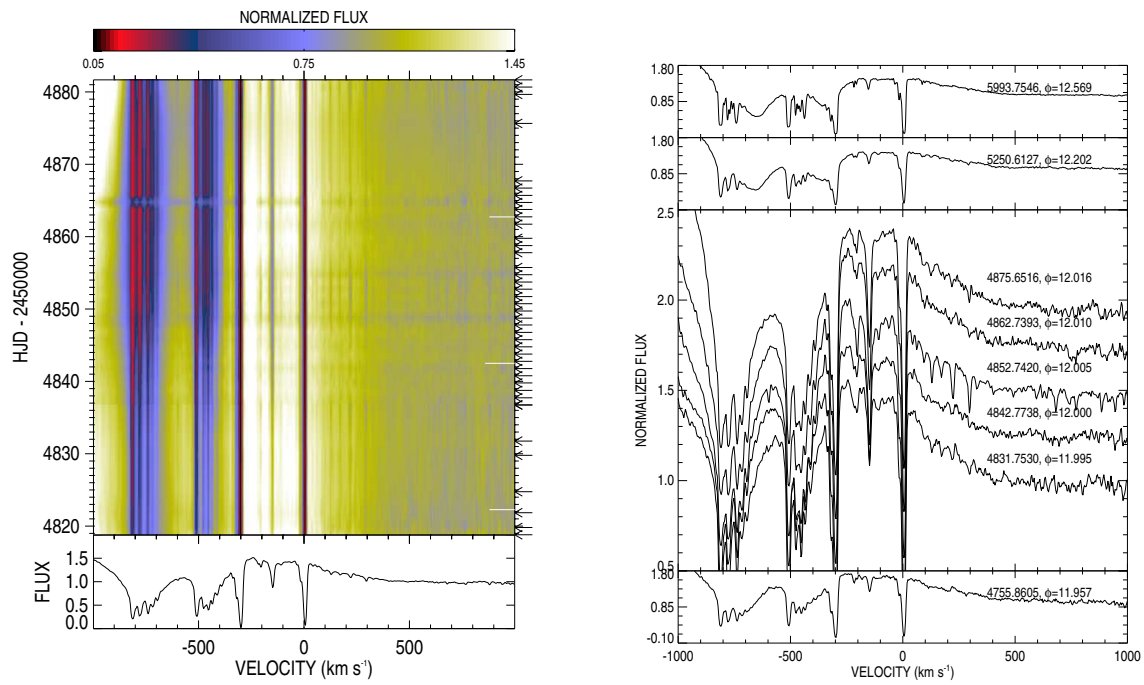


Fig. 1.12.— Dynamical (left) and line plots (right) of Na I D₁ λ 5896 during the 2009 event. The white horizontal bars on the dynamical representation indicate phases 11.99, 12.00, and 12.01.

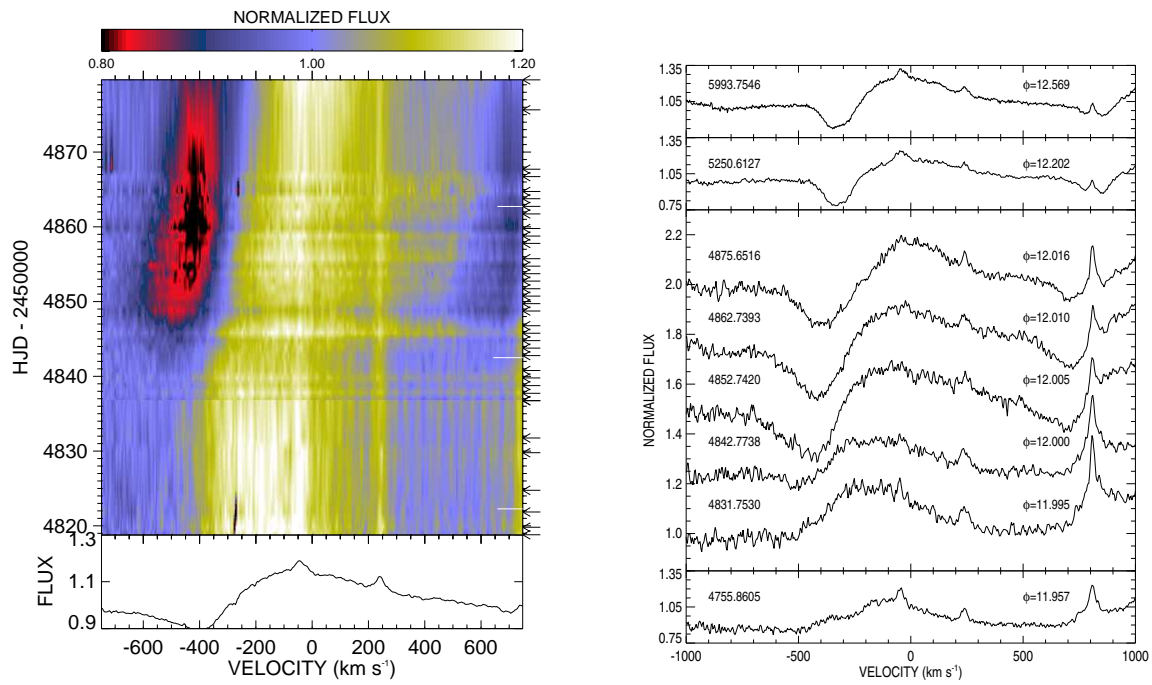


Fig. 1.13.— Dynamical (left) and line plots (right) of Si II $\lambda 6347$ during the 2009 event. The white horizontal bars on the dynamical representation indicate phases 11.99, 12.00, and 12.01.

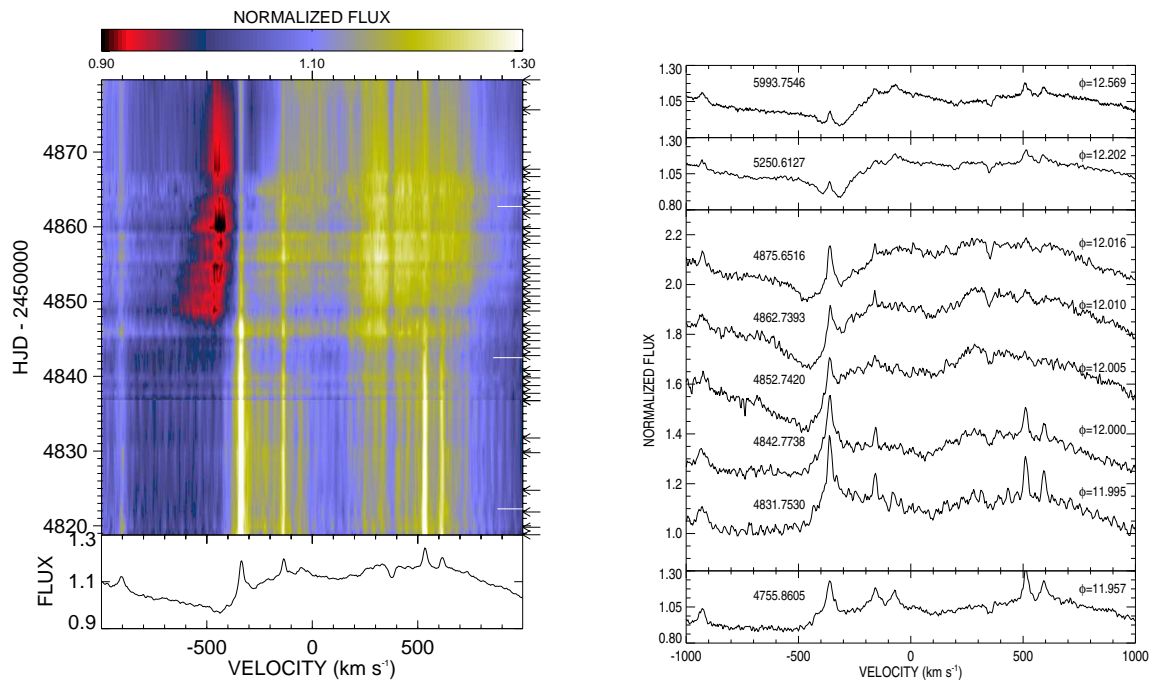


Fig. 1.14.— Dynamical (left) and line plots (right) of Si II $\lambda 6371$ during the 2009 event. The white horizontal bars on the dynamical representation indicate phases 11.99, 12.00, and 12.01.

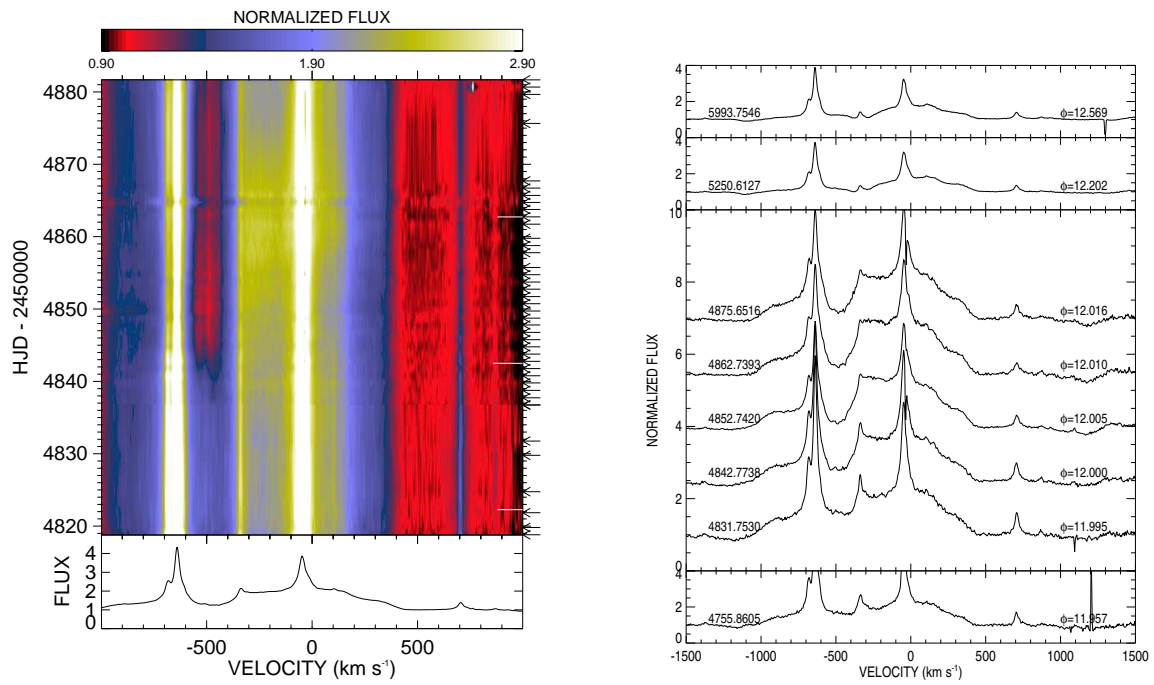


Fig. 1.15.— Dynamical (left) and line plots (right) of Fe II $\lambda 5169$ during the 2009 event. The white horizontal bars on the dynamical representation indicate phases 11.99, 12.00, and 12.01.

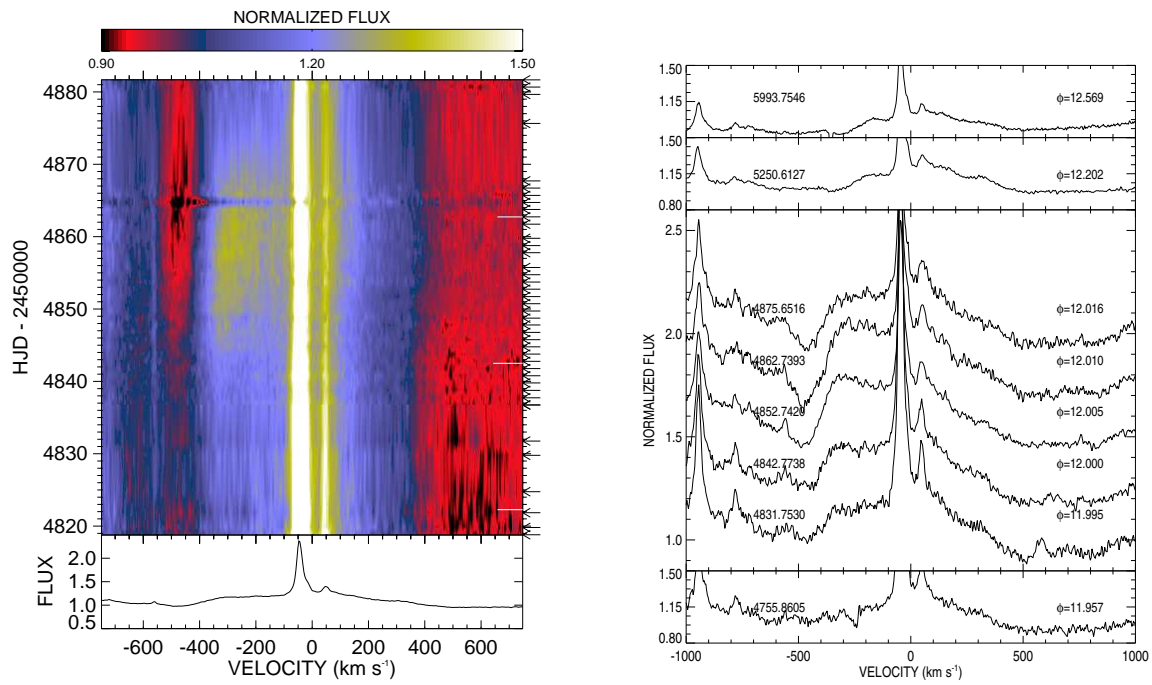


Fig. 1.16.— Dynamical (left) and line plots (right) of Fe II $\lambda 5197$ during the 2009 event. The white horizontal bars on the dynamical representation indicate phases 11.99, 12.00, and 12.01.

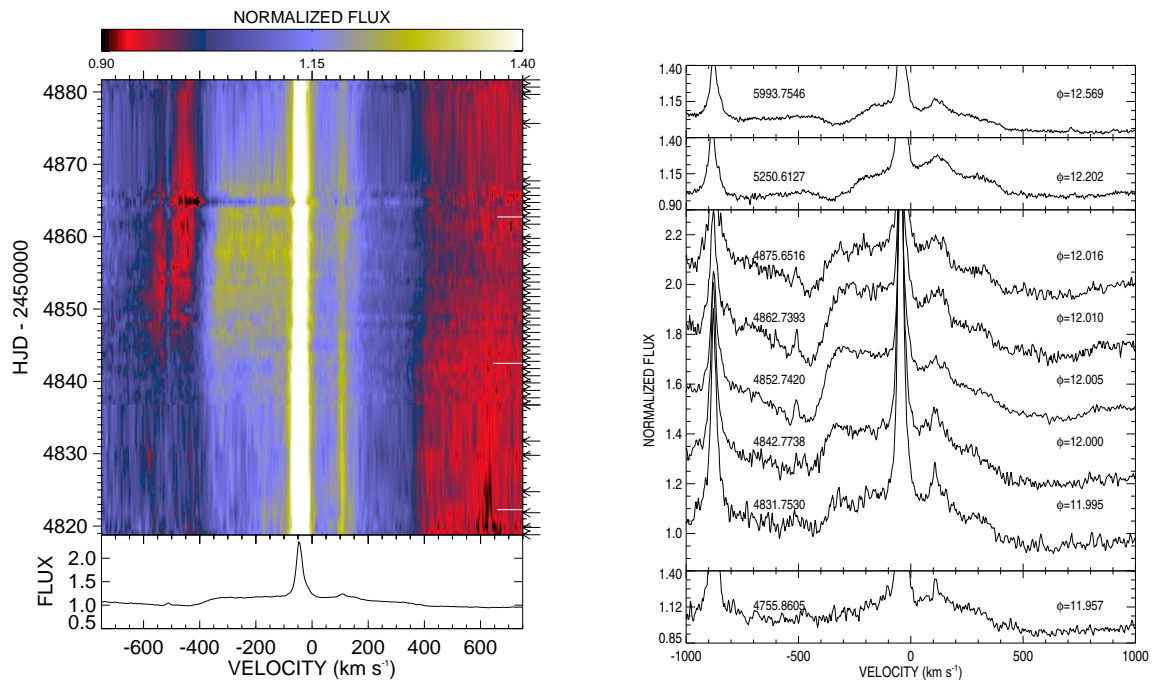


Fig. 1.17.— Dynamical (left) and line plots (right) of Fe II $\lambda 5234$ during the 2009 event. The white horizontal bars on the dynamical representation indicate phases 11.99, 12.00, and 12.01.

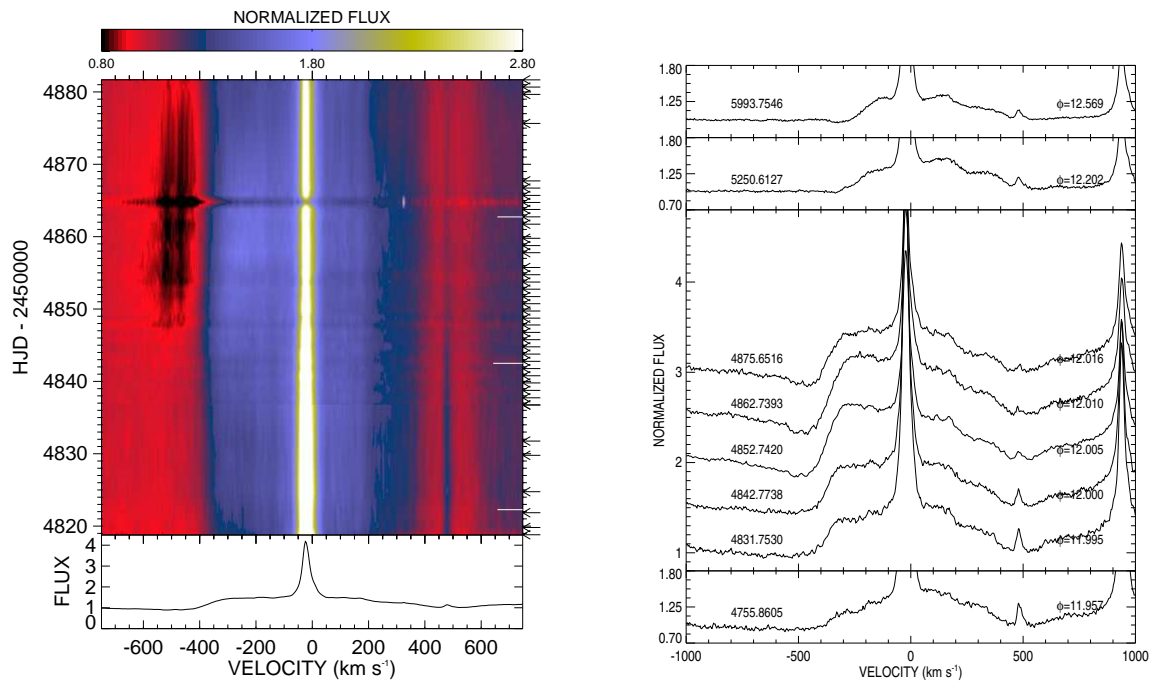


Fig. 1.18.— Dynamical (left) and line plots (right) of Fe II $\lambda 5316$ during the 2009 event. The white horizontal bars on the dynamical representation indicate phases 11.99, 12.00, and 12.01.

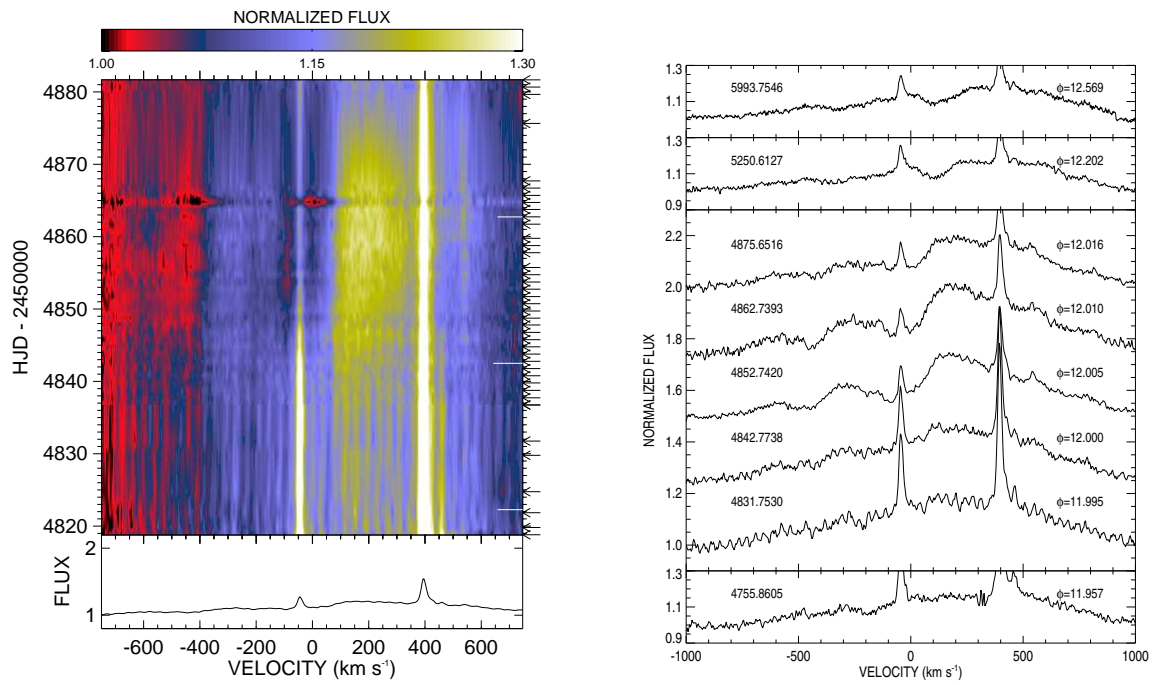


Fig. 1.19.— Dynamical (left) and line plots (right) of Fe II $\lambda 6238$ during the 2009 event. The white horizontal bars on the dynamical representation indicate phases 11.99, 12.00, and 12.01.

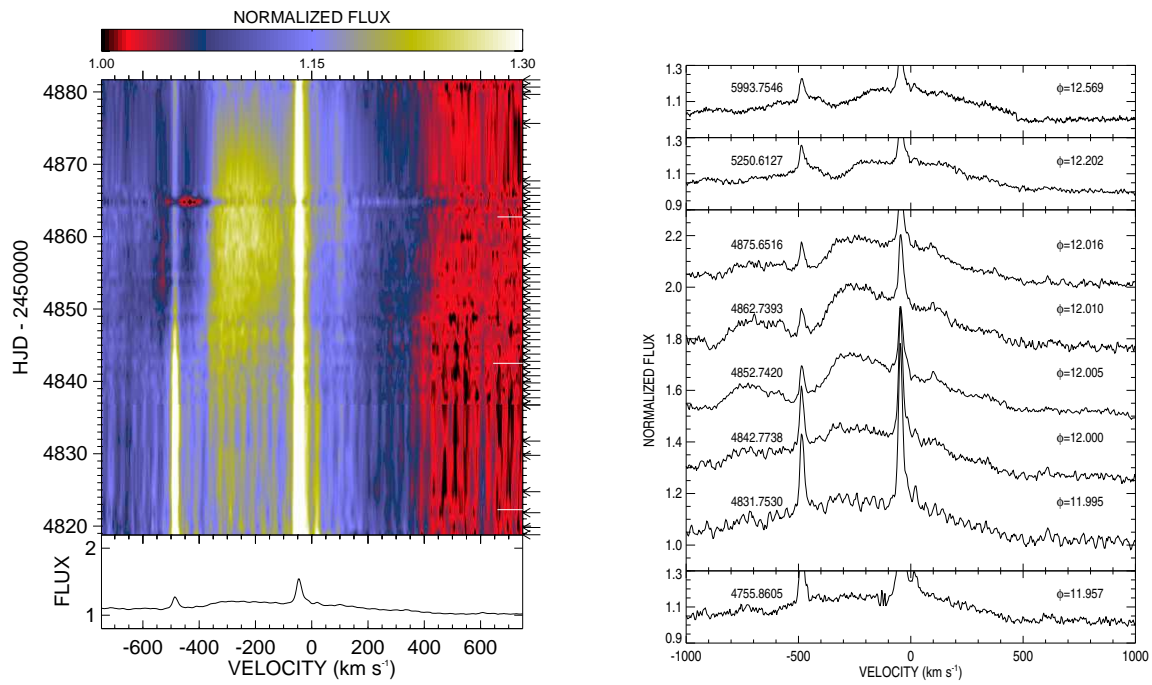


Fig. 1.20.— Dynamical (left) and line plots (right) of Fe II $\lambda 6248$ during the 2009 event. The white horizontal bars on the dynamical representation indicate phases 11.99, 12.00, and 12.01.

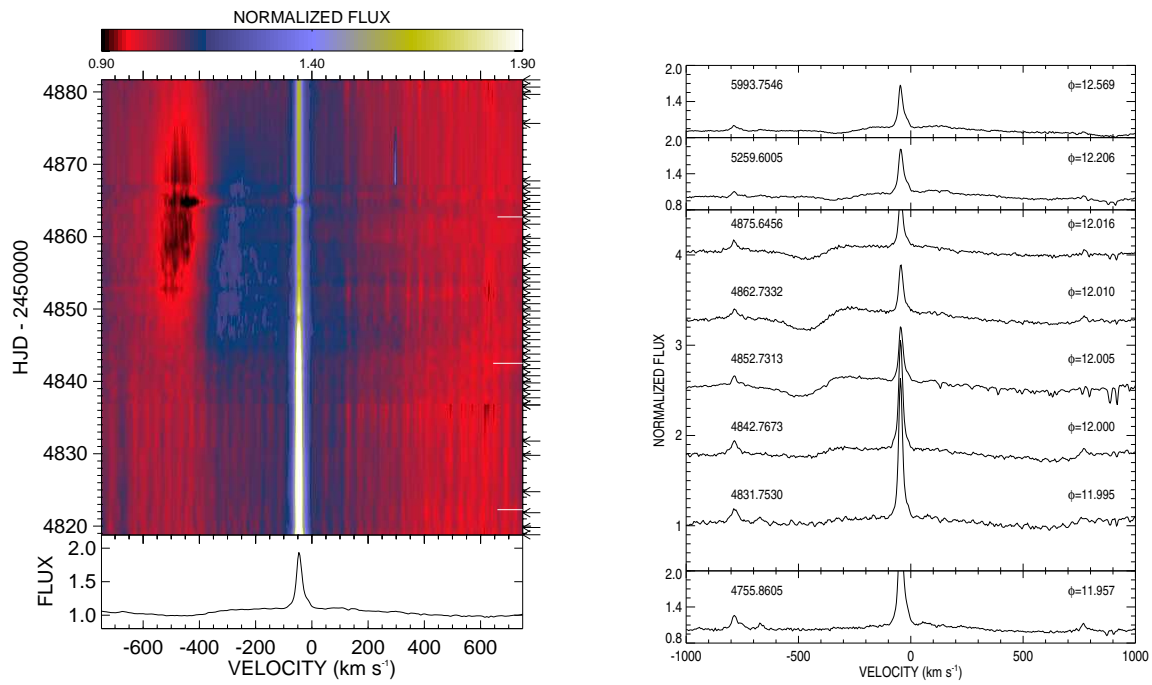


Fig. 1.21.— Dynamical (left) and line plots (right) of Fe II $\lambda 6456$ during the 2009 event. The white horizontal bars on the dynamical representation indicate phases 11.99, 12.00, and 12.01.

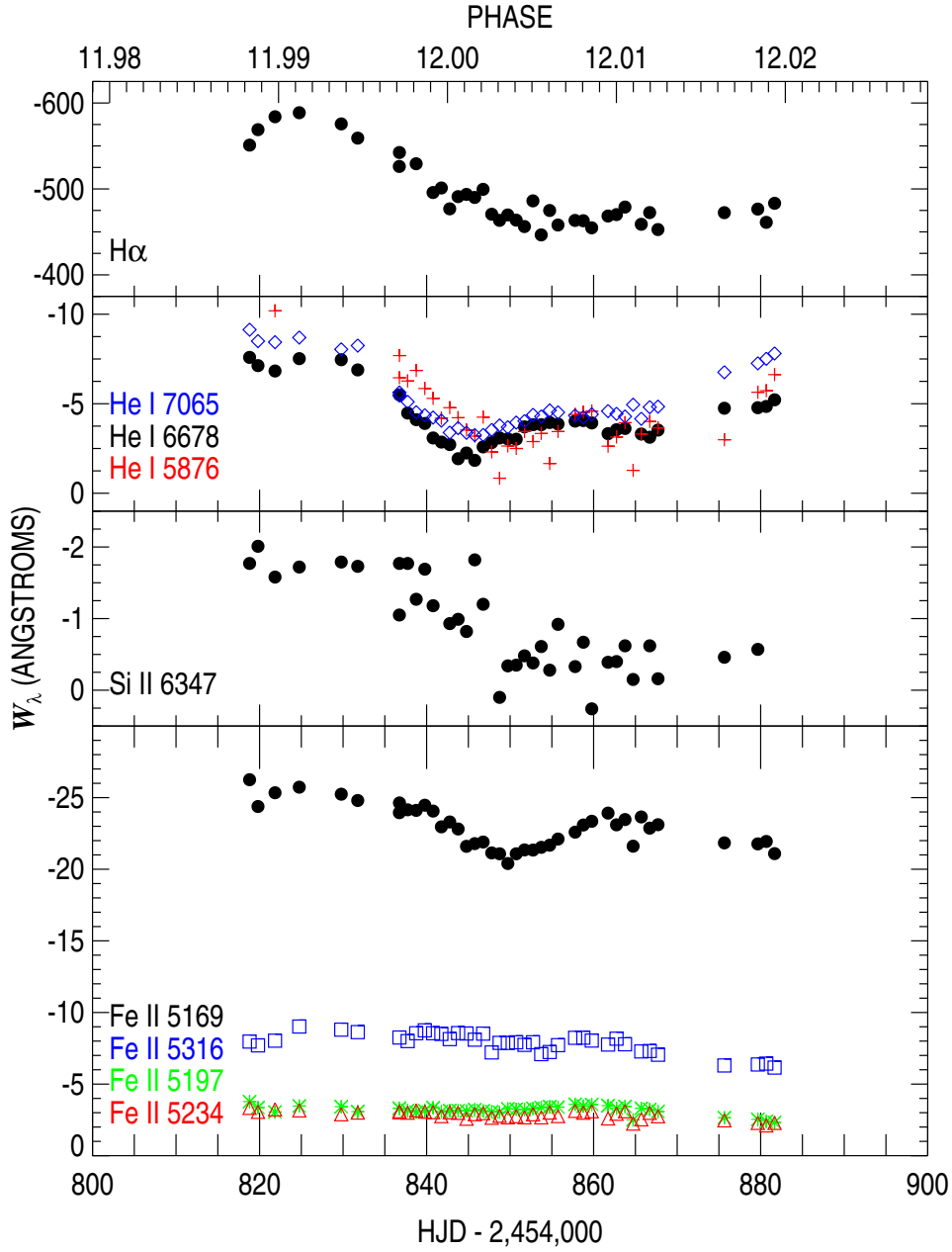


Fig. 2.— Equivalent width measurements from our echelle data across the 2009 event.

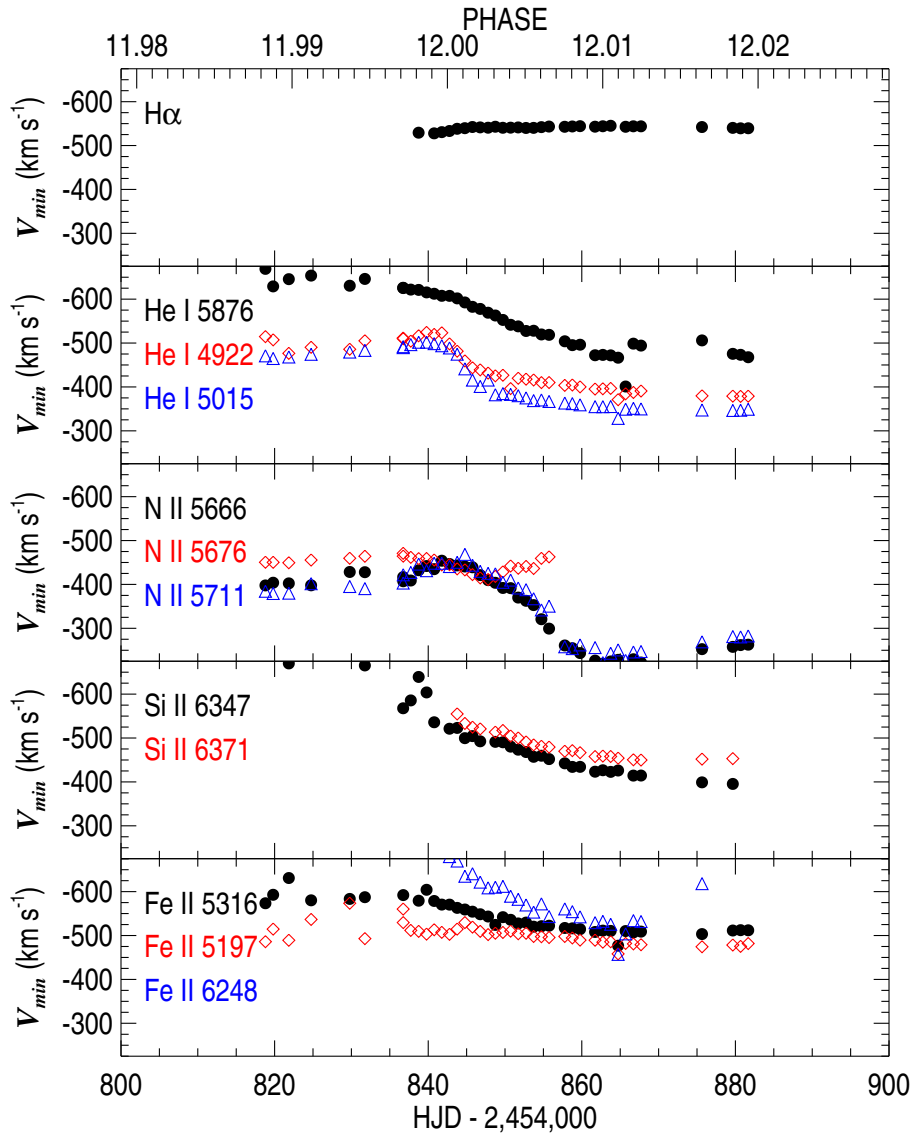


Fig. 3.— Measurements of radial velocities of the P Cygni absorption components, V_{min} .

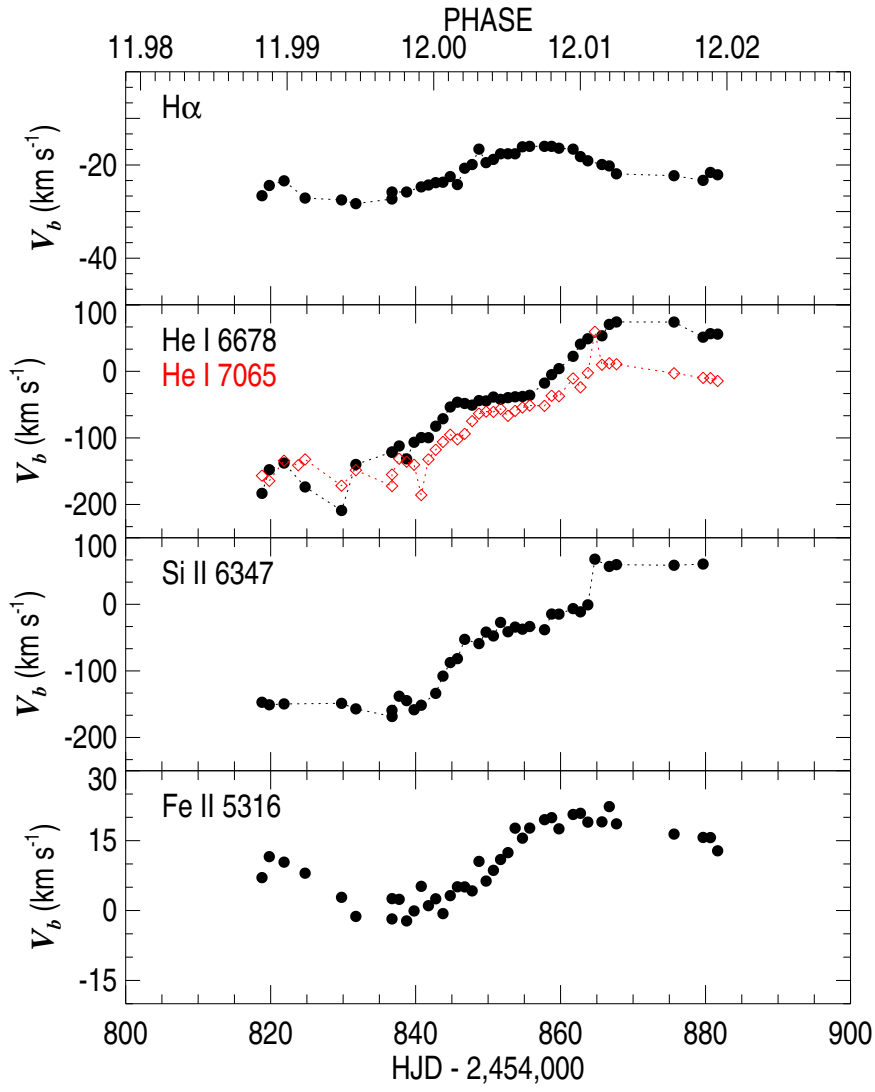


Fig. 4.— Measurements of emission line bisector radial velocities, V_b . The bisector velocities for $\text{H}\alpha$ from Paper 1 are shown for comparison, and each emission line is marked.

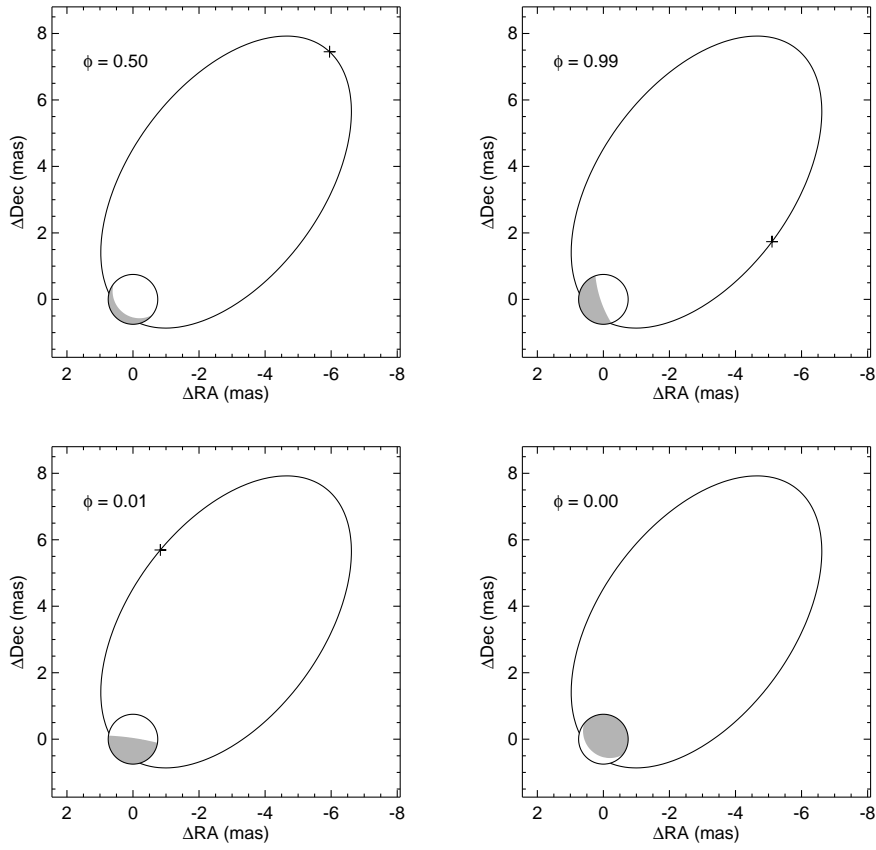


Fig. 5.— A depiction of the relative astrometric orbit of the companion in the plane of the sky. The four panels show the orientation of the primary and secondary stars at different orbital phases (arranged in a clockwise order), where the primary star’s wind is illuminated by the secondary (white is illuminated, grey is not).

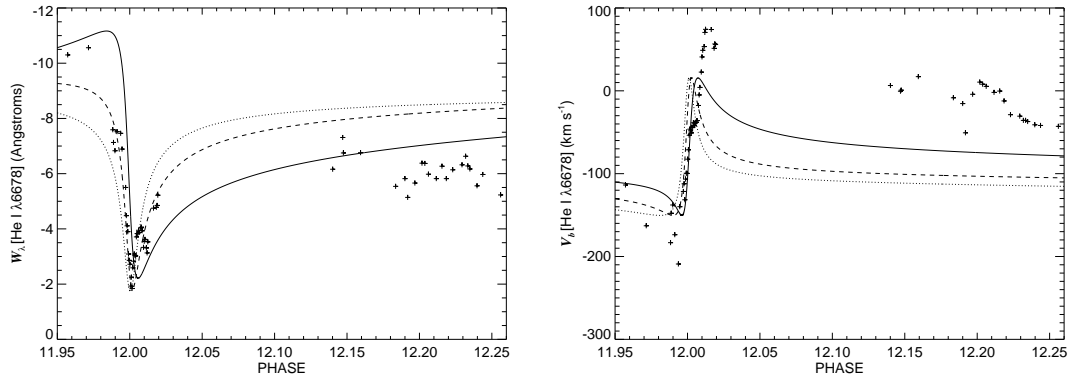


Fig. 6.— The temporal variations in the He I $\lambda 6678$ equivalent width (left panel) and emission peak bisector velocity (right panel) compared with predictions of the illuminated hemisphere model. The three lines correspond to trial models with a longitude of periastron ω_p equal to 200° (dotted line), 240° (dashed line), and 263° (solid line). Deviations from the fits at later time (phase 12.2) may be related to the presence then of strong P Cygni absorption which reduces the emission equivalent width and shifts the emission line bisector to more positive values.

Table 1. Optical Wind Line Parameters^a

Species	Rest Wavelength (Å)	Ionization Energy (eV)	Energy E_{lower} (eV)	Energy E_{upper} (eV)	Blue Int. Limit (km s ⁻¹)	Red Int. Limit (km s ⁻¹)	Figure Set Number	Line Blends ^b
H I(H β)	4861.33	13.598	10.2028	12.7535	1	W, LHA
H I(H α)	6562.82	13.598	10.2028	12.0922	-2500	+2500	2	W, LHA, [N II] 6548, 6583
He I	4921.93	24.587	21.2180	23.7357	-800	+800	3	W, Fe II 4922
He I	5015.68	24.587	20.6152	23.0864	-1000	+1000	4	W, Fe II 5015
He I	5875.62	24.587	20.9723	23.0827	-1000	+2000	5	W, [Fe II], Na D1, D2
He I	6678.15	24.587	21.2263	23.0831	-1000	+1000	6	W, [Ni II]
He I	7065.19	24.587	21.2263	22.7273	-1000	+1000	7	W, telluric
N II	5666.63	29.601	18.4734	20.6616	8	Fe II 5658
N II	5676.02	29.601	18.4695	20.6541	9	[Fe II] 5674
N II	5710.77	29.601	18.4903	20.6616	10	
Na I D ₂	5889.95	5.139	0.0000	2.1044	11	LHA, HA
Na I D ₁	5895.92	5.139	0.0000	2.1022	12	LHA, HA
Si II	6347.10	16.346	8.1242	10.0778	-1000	+400	13	W, [Fe II] 6355
Si II	6371.36	16.346	8.1242	10.0704	14	W, Fe II 6371 (wind), Fe II 6384, 6386 (nebular)
Fe II	5169.03	16.199	2.8922	5.2910	-2500	+2500	15	W, [Fe II] 5158, 5159, 5164
Fe II	5197.58	16.199	3.2304	5.6151	-700	+700	16	
Fe II	5234.63	16.199	3.2226	5.5914	-2500	+2500	17	W, Ti II 5228
Fe II	5316.23	16.199	3.1528	5.4841	-700	+650	18	
Fe II	6238.38	16.199	3.8886	5.8754	19	
Fe II	6247.56	16.199	3.8915	5.8754	20	

Table 1—Continued

Species	Rest Wavelength (Å)	Ionization Energy (eV)	Energy E_{lower} (eV)	Energy E_{upper} (eV)	Blue Int. Limit (km s ⁻¹)	Red Int. Limit (km s ⁻¹)	Figure Set Number	Line Blends ^b
Fe II	6456.38	16.199	3.8931	5.8779	21	W, Fe II 6446

^aAtomic data collected from NIST (<http://nist.gov/pml/data/asd.cfm>).

^bA ‘W’ indicates a Weigelt knot contamination from the same transition, which dominates the narrow emission component. ‘LHA’ indicates “anomalous absorption”, which is from intervening gas located in the Little Homunculus, while ‘HA’ refers to absorption from the intervening gas of the Homunculus.

Table 2. Wind Line Measurements. - complete table to only be online

Ion / Line	HJD -2,454,000	Phase	W_λ (Å)	V_{\min} (km s ⁻¹)	V_b (km s ⁻¹)
H α	784.858	11.971	-650.3	-723.7	-18.1
H α	818.806	11.988	-551.0	-735.1	-26.6
H α	819.811	11.989	-568.9	-757.2	-24.4
H α	821.852	11.989	-584.0	-755.3	-23.4
H α	824.754	11.991	-588.7	-768.3	-27.1
H α	829.784	11.994	-575.6	-790.3	-27.5
H α	831.753	11.995	-559.1	-791.9	-28.3
H α	836.744	11.997	-542.4	-1028.7	-25.8
H α	838.750	11.998	-529.3	-529.3	-25.8
H α	840.772	11.999	-495.8	-527.8	-24.7
H α	841.768	12.000	-501.1	-530.6	-24.3
H α	842.767	12.000	-476.8	-533.2	-23.8
H α	843.767	12.001	-491.0	-538.2	-23.7
H α	844.769	12.001	-493.6	-539.6	-22.5
H α	845.758	12.002	-490.1	-542.3	-24.2
H α	846.761	12.002	-499.5	-541.4	-20.7
H α	847.797	12.003	-470.5	-540.7	-19.9
H α	848.735	12.003	-463.4	-542.9	-16.6
H α	849.715	12.004	-469.7	-540.5	-19.5
H α	850.727	12.004	-463.7	-540.8	-18.8
H α	851.713	12.005	-456.2	-541.3	-17.6
H α	852.731	12.005	-486.1	-540.1	-17.6
H α	853.722	12.006	-446.5	-540.3	-17.6
H α	854.734	12.006	-474.9	-542.0	-16.1
H α	855.728	12.007	-458.0	-543.3	-16.0
H α	857.771	12.008	-463.3	-542.8	-16.0
H α	858.760	12.008	-463.0	-543.5	-16.0
H α	859.768	12.009	-454.7	-544.2	-16.4
H α	861.721	12.010	-468.5	-543.0	-16.6
H α	862.733	12.010	-470.1	-544.0	-18.2

Table 2—Continued

Ion / Line	HJD -2,454,000	Phase	W_λ (Å)	V_{\min} (km s ⁻¹)	V_b (km s ⁻¹)
H α	863.753	12.011	-478.9	-545.1	-19.1
H α	865.703	12.011	-458.8	-542.8	-19.9
H α	866.710	12.012	-472.5	-543.9	-20.2
H α	867.701	12.012	-452.7	-543.8	-21.9
H α	875.646	12.016	-472.4	-542.2	-22.3
H α	879.654	12.018	-476.5	-540.3	-23.3
H α	880.672	12.019	-461.1	-539.3	-21.6
H α	881.668	12.019	-483.3	-539.4	-22.1
He I 4922	755.860	11.957	-13.69	-456.8	81.9
He I 4922	784.858	11.972	-10.36	-420.8	73.8
He I 4922	818.806	11.988	-14.57	-514.6	84.2
He I 4922	819.811	11.989	-12.85	-507.3	89.6
He I 4922	821.852	11.990	-13.37	-476.5	72.4
He I 4922	824.754	11.991	-11.77	-490.3	45.9
He I 4922	829.784	11.994	-11.55	-485.8	72.8
He I 4922	831.753	11.995	-12.08	-505.2	65.1
He I 4922	836.751	11.997	-11.48	-509.8	64.8
He I 4922	836.738	11.997	-11.67	-511.4	64.3
He I 4922	837.732	11.998	-11.09	-504.3	48.0
He I 4922	838.757	11.998	-10.54	-516.6	44.1
He I 4922	839.787	11.999	-11.09	-524.2	45.8
He I 4922	840.779	11.999	-11.54	-519.7	45.4
He I 4922	841.768	12.000	-11.42	-523.4	32.8
He I 4922	842.774	12.000	-10.05	-498.2	38.0
He I 4922	843.774	12.001	-10.71	-481.4	39.8
He I 4922	844.776	12.001	-10.23	-459.4	26.3
He I 4922	845.765	12.002	-9.40	-443.6	24.7
He I 4922	846.770	12.002	-9.80	-438.8	23.4
He I 4922	847.797	12.003	-10.73	-431.6	21.2
He I 4922	848.741	12.003	-8.91	-425.3	29.7

Table 2—Continued

Ion / Line	HJD -2,454,000	Phase	W_λ (Å)	V_{\min} (km s ⁻¹)	V_b (km s ⁻¹)
He I 4922	849.726	12.004	-9.43	-426.7	17.7
He I 4922	850.733	12.004	-9.53	-396.3	16.2
He I 4922	851.719	12.005	-9.44	-419.8	21.5
He I 4922	852.742	12.005	-9.13	-417.7	19.7
He I 4922	853.728	12.006	-10.6	-415.8	17.6
He I 4922	854.740	12.006	-9.71	-409.9	28.2
He I 4922	855.736	12.007	-9.10	-410.1	30.3
He I 4922	857.786	12.008	-9.55	-403.6	32.8
He I 4922	858.768	12.008	-9.40	-404.4	44.0
He I 4922	859.775	12.009	-9.03	-400.1	31.6
He I 4922	861.727	12.010	-10.31	-395.2	45.1
He I 4922	862.739	12.010	-9.97	-395.8	46.6
He I 4922	863.759	12.011	-9.40	-396.6	64.4
He I 4922	864.728	12.011	-9.22	-370.9	87.6
He I 4922	865.703	12.011	-10.57	-384.4	59.9
He I 4922	866.717	12.012	-8.96	-387.4	79.8
He I 4922	867.708	12.012	-9.28	-390.7	74.5
He I 4922	875.652	12.016	-8.23	-379.7	87.5
He I 4922	879.661	12.018	-7.74	-379.0	87.8
He I 4922	880.672	12.019	-7.71	-378.5	...
He I 4922	881.668	12.019	-8.08	-378.9	89.6
He I 5015	755.860	11.957	-20.90	-440.3	108.5
He I 5015	784.858	11.972	-13.12	-436.0	123.5
He I 5015	818.806	11.988	-23.25	-470.8	86.7
He I 5015	819.811	11.989	-18.97	-464.8	80.7
He I 5015	821.852	11.990	-18.72	-468.2	88.0
He I 5015	824.754	11.991	-18.96	-474.4	91.5
He I 5015	829.784	11.994	-18.19	-479.4	84.8
He I 5015	831.753	11.995	-19.36	-483.3	72.6
He I 5015	836.751	11.997	-16.31	-489.5	98.2

Table 2—Continued

Ion / Line	HJD -2,454,000	Phase	W_λ (Å)	V_{\min} (km s ⁻¹)	V_b (km s ⁻¹)
He I 5015	836.738	11.997	-17.26	-491.7	94.8
He I 5015	837.732	11.998	-16.33	-496.4	98.3
He I 5015	838.757	11.998	-15.75	-501.8	95.3
He I 5015	839.787	11.999	-16.32	-502.0	97.5
He I 5015	840.779	11.999	-16.63	-498.7	95.8
He I 5015	841.768	12.000	-14.47	-493.8	95.8
He I 5015	842.774	12.000	-16.11	-488.8	96.9
He I 5015	843.774	12.001	-16.69	-474.7	92.5
He I 5015	844.776	12.001	-15.82	-441.2	93.2
He I 5015	845.765	12.002	-16.46	-415.6	92.6
He I 5015	846.770	12.002	-17.97	-401.1	87.5
He I 5015	847.797	12.003	-17.47	-415.7	95.4
He I 5015	848.741	12.003	-16.57	-382.1	106.4
He I 5015	849.726	12.004	-17.54	-384.9	91.9
He I 5015	850.733	12.004	-17.43	-383.0	97.9
He I 5015	851.719	12.005	-16.95	-380.0	98.5
He I 5015	852.742	12.005	-17.44	-375.0	98.1
He I 5015	853.728	12.006	-19.42	-368.9	104.3
He I 5015	854.740	12.006	-17.90	-370.3	105.3
He I 5015	855.736	12.007	-18.76	-366.9	104.1
He I 5015	857.786	12.008	-18.58	-363.3	109.3
He I 5015	858.768	12.008	-19.53	-362.0	107.2
He I 5015	859.775	12.009	-18.77	-359.2	116.9
He I 5015	861.727	12.010	-18.51	-355.1	118.2
He I 5015	862.739	12.010	-18.20	-355.0	120.5
He I 5015	863.759	12.011	-19.90	-355.3	119.0
He I 5015	864.728	12.011	-17.27	-328.4	150.3
He I 5015	865.703	12.011	-21.39	-349.3	122.0
He I 5015	866.717	12.012	-19.34	-351.2	122.6
He I 5015	867.708	12.012	-18.35	-349.9	124.6

Table 2—Continued

Ion / Line	HJD -2,454,000	Phase	W_λ (Å)	V_{\min} (km s ⁻¹)	V_b (km s ⁻¹)
He I 5015	875.652	12.016	-16.39	-347.4	132.3
He I 5015	879.661	12.018	-15.96	-346.4	125.5
He I 5015	880.672	12.019	-14.24	-346.9	125.4
He I 5015	881.668	12.019	-14.98	-349.2	121.8
He I 5876	755.860	11.957	-24.87	-551.2	-207.4
He I 5876	784.858	11.972	-27.94	-618.3	-208.5
He I 5876	818.806	11.988	-13.52	-669.0	-211.4
He I 5876	819.811	11.989	-11.06	-629.1	-214.4
He I 5876	821.852	11.990	-10.19	-645.6	-214.7
He I 5876	824.754	11.991	-11.64	-653.7	-213.9
He I 5876	829.784	11.994	-11.28	-630.6	-214.1
He I 5876	831.753	11.995	-11.13	-646.1	-215.5
He I 5876	836.751	11.997	-7.690	-625.3	-216.8
He I 5876	836.738	11.997	-6.450	-626.0	-218.2
He I 5876	837.732	11.998	-6.270	-621.8	-218.7
He I 5876	838.757	11.998	-6.860	-621.1	-219.6
He I 5876	839.787	11.999	-5.850	-615.4	-219.7
He I 5876	840.779	11.999	-5.300	-612.3	-219.9
He I 5876	841.768	12.000	-4.190	-607.6	-220.6
He I 5876	842.774	12.000	-4.780	-607.5	-220.7
He I 5876	843.774	12.001	-4.220	-601.8	-221.7
He I 5876	844.776	12.001	-3.530	-592.5	-222.4
He I 5876	845.765	12.002	-3.190	-582.5	-222.8
He I 5876	846.770	12.002	-4.250	-577.8	-222.1
He I 5876	847.797	12.003	-2.310	-569.1	-223.0
He I 5876	848.741	12.003	-0.840	-562.8	-223.6
He I 5876	849.726	12.004	-2.640	-552.7	-222.1
He I 5876	850.733	12.004	-2.500	-541.6	-222.5
He I 5876	851.719	12.005	-3.450	-538.0	-223.0
He I 5876	852.742	12.005	-2.890	-527.5	-223.0

Table 2—Continued

Ion / Line	HJD -2,454,000	Phase	W_λ (Å)	V_{\min} (km s ⁻¹)	V_b (km s ⁻¹)
He I 5876	853.728	12.006	-3.340	-528.0	-223.6
He I 5876	854.740	12.006	-1.660	-519.6	-221.8
He I 5876	855.736	12.007	-3.450	-518.7	-222.8
He I 5876	857.786	12.008	-4.400	-504.0	-222.9
He I 5876	858.768	12.008	-4.530	-495.2	-222.8
He I 5876	859.775	12.009	-4.590	-496.2	-222.3
He I 5876	861.727	12.010	-2.630	-472.2	-220.5
He I 5876	862.739	12.010	-3.140	-473.0	-220.5
He I 5876	863.759	12.011	-3.940	-471.9	-220.0
He I 5876	864.728	12.011	-1.280	-466.6	-224.4
He I 5876	865.703	12.011	-3.310	-401.0	-220.4
He I 5876	866.717	12.012	-4.010	-498.6	-218.6
He I 5876	867.708	12.012	-3.650	-494.2	-218.3
He I 5876	875.652	12.016	-2.990	-506.0	-215.4
He I 5876	879.661	12.018	-5.640	-475.4	-214.8
He I 5876	880.672	12.019	-5.730	-473.2	-213.9
He I 5876	881.668	12.019	-6.630	-467.7	-213.9
He I 6678	755.860	11.957	-10.30	...	-113.7
He I 6678	784.858	11.972	-10.56	...	-162.9
He I 6678	818.806	11.988	-7.59	...	-183.3
He I 6678	819.811	11.989	-7.13	...	-147.8
He I 6678	821.852	11.990	-6.83	...	-137.8
He I 6678	824.754	11.991	-7.52	...	-173.7
He I 6678	829.784	11.994	-7.46	...	-209.06
He I 6678	831.753	11.995	-6.89	...	-139.9
He I 6678	836.751	11.997	-5.50	...	-121.5
He I 6678	837.732	11.998	-4.48	...	-112.2
He I 6678	838.757	11.998	-4.11	...	-131.5
He I 6678	839.787	11.999	-3.90	...	-106.6
He I 6678	840.779	11.999	-3.09	...	-99.5

Table 2—Continued

Ion / Line	HJD -2,454,000	Phase	W_λ (Å)	V_{\min} (km s ⁻¹)	V_b (km s ⁻¹)
He I 6678	841.768	12.000	-2.86	...	-99.7
He I 6678	842.774	12.000	-2.72	...	-82.5
He I 6678	843.774	12.001	-1.93	...	-71.2
He I 6678	844.776	12.001	-2.25	...	-53.6
He I 6678	845.765	12.002	-1.84	...	-46.3
He I 6678	846.770	12.002	-2.59	...	-48.3
He I 6678	847.797	12.003	-2.83	...	-50.8
He I 6678	848.741	12.003	-3.09	...	-43.9
He I 6678	849.726	12.004	-3.04	...	-44.2
He I 6678	850.733	12.004	-3.02	...	-38.6
He I 6678	851.719	12.005	-3.71	...	-42.1
He I 6678	852.742	12.005	-3.83	...	-39.5
He I 6678	853.728	12.006	-3.83	...	-38.3
He I 6678	854.740	12.006	-3.95	...	-37.8
He I 6678	855.736	12.007	-3.87	...	-35.9
He I 6678	857.786	12.008	-4.03	...	-17.7
He I 6678	858.768	12.008	-4.06	...	-4.98
He I 6678	859.775	12.009	-3.93	...	4.1
He I 6678	861.727	12.010	-3.33	...	22.6
He I 6678	862.739	12.010	-3.55	...	40.9
He I 6678	863.759	12.011	-3.62	...	48.9
He I 6678	865.703	12.011	-3.31	...	53.4
He I 6678	866.717	12.012	-3.13	...	70.5
He I 6678	867.708	12.012	-3.53	...	74.2
He I 6678	875.652	12.016	-4.75	...	74.0
He I 6678	879.661	12.018	-4.78	...	51.3
He I 6678	880.672	12.019	-4.85	...	56.6
He I 6678	881.668	12.019	-5.22	...	55.9
He I 6678	1125.868	12.140	-6.16	...	6.4
He I 6678	1139.844	12.147	-7.31	...	-0.5

Table 2—Continued

Ion / Line	HJD -2,454,000	Phase	W_λ (Å)	V_{\min} (km s ⁻¹)	V_b (km s ⁻¹)
He I 6678	1140.825	12.147	-6.75	...	0.8
He I 6678	1164.812	12.159	-6.76	...	17.1
He I 6678	1213.759	12.184	-5.54	...	-8.4
He I 6678	1226.740	12.190	-5.82	...	-15.4
He I 6678	1230.625	12.192	-5.14	...	-50.7
He I 6678	1240.647	12.197	-5.66	...	-4.2
He I 6678	1250.613	12.202	-6.38	...	10.5
He I 6678	1254.575	12.204	-6.37	...	8.0
He I 6678	1259.604	12.206	-5.98	...	5.4
He I 6678	1270.556	12.212	-5.82	...	-1.9
He I 6678	1278.498	12.216	-6.27	...	-0.3
He I 6678	1284.535	12.219	-5.82	...	-12.2
He I 6678	1293.510	12.223	-6.14	...	-28.8
He I 6678	1306.501	12.229	-6.32	...	-30.6
He I 6678	1311.519	12.232	-6.63	...	-35.7
He I 6678	1314.597	12.233	-6.28	...	-35.7
He I 6678	1317.486	12.235	-6.17	...	-37.1
He I 6678	1327.462	12.240	-5.56	...	-41.0
He I 6678	1335.475	12.244	-5.97	...	-41.8
He I 6678	1360.372	12.256	-5.23	...	-42.9
He I 7065	755.860	11.957	-16.18	...	-119.1
He I 7065	784.858	11.972	-11.99	...	-123.6
He I 7065	818.806	11.988	-9.14	...	-156.7
He I 7065	819.811	11.989	-8.50	...	-164.5
He I 7065	821.852	11.990	-8.44	...	-134.2
He I 7065	824.754	11.991	-8.70	...	-132.3
He I 7065	829.784	11.994	-8.04	...	-171.8
He I 7065	831.753	11.995	-8.25	...	-148.5
He I 7065	836.751	11.997	-5.63	...	-172.3
He I 7065	836.738	11.997	-5.46	...	-155.1

Table 2—Continued

Ion / Line	HJD -2,454,000	Phase	W_λ (Å)	V_{\min} (km s ⁻¹)	V_b (km s ⁻¹)
He I 7065	837.732	11.998	-5.11	...	-131.2
He I 7065	838.757	11.998	-4.53	...	-135.8
He I 7065	839.787	11.999	-4.36	...	-140.4
He I 7065	840.779	11.999	-4.23	...	-185.8
He I 7065	841.768	12.000	-4.06	...	-132.3
He I 7065	842.774	12.000	-3.39	...	-117.8
He I 7065	843.774	12.001	-3.64	...	-106.0
He I 7065	844.776	12.001	-3.38	...	-95.1
He I 7065	845.765	12.002	-3.25	...	-102.1
He I 7065	846.770	12.002	-3.26	...	-93.8
He I 7065	847.797	12.003	-3.54	...	-74.9
He I 7065	848.741	12.003	-3.79	...	-63.5
He I 7065	849.726	12.004	-3.69	...	-60.5
He I 7065	850.733	12.004	-3.95	...	-60.9
He I 7065	851.719	12.005	-4.03	...	-56.5
He I 7065	852.742	12.005	-4.38	...	-66.8
He I 7065	853.728	12.006	-4.29	...	-59.4
He I 7065	854.740	12.006	-4.63	...	-54.3
He I 7065	855.736	12.007	-4.52	...	-51.3
He I 7065	857.786	12.008	-4.34	...	-51.8
He I 7065	858.768	12.008	-4.24	...	-36.8
He I 7065	859.775	12.009	-4.41	...	-37.3
He I 7065	861.727	12.010	-4.59	...	-10.6
He I 7065	862.739	12.010	-4.44	...	-23.9
He I 7065	863.759	12.011	-4.29	...	-2.3
He I 7065	864.728	12.011	-4.95	...	59.5
He I 7065	865.703	12.011	-4.16	...	9.9
He I 7065	866.717	12.012	-4.81	...	12.2
He I 7065	867.708	12.012	-4.84	...	10.7
He I 7065	875.652	12.016	-6.76	...	-2.9

Table 2—Continued

Ion / Line	HJD -2,454,000	Phase	W_λ (Å)	V_{\min} (km s ⁻¹)	V_b (km s ⁻¹)
He I 7065	879.661	12.018	-7.26	...	-9.8
He I 7065	880.672	12.019	-7.51	...	-10.2
He I 7065	881.668	12.019	-7.81	...	-14.5
N II 5666	755.860	11.957	...	-318.6	...
N II 5666	784.858	11.972	...	-390.8	...
N II 5666	818.806	11.988	...	-397.7	...
N II 5666	819.811	11.989	...	-403.9	...
N II 5666	821.852	11.990	...	-402.4	...
N II 5666	824.754	11.991	...	-398.0	...
N II 5666	829.784	11.994	...	-428.4	...
N II 5666	831.753	11.995	...	-427.9	...
N II 5666	836.751	11.997	...	-407.2	...
N II 5666	836.738	11.997	...	-416.6	...
N II 5666	837.732	11.998	...	-408.9	...
N II 5666	838.757	11.998	...	-432.4	...
N II 5666	839.787	11.999	...	-441.9	...
N II 5666	840.779	11.999	...	-434.8	...
N II 5666	841.768	12.000	...	-454.0	...
N II 5666	842.774	12.000	...	-446.5	...
N II 5666	843.774	12.001	...	-443.3	...
N II 5666	844.776	12.001	...	-440.8	...
N II 5666	845.765	12.002	...	-439.1	...
N II 5666	846.770	12.002	...	-421.2	...
N II 5666	847.797	12.003	...	-409.8	...
N II 5666	848.741	12.003	...	-403.7	...
N II 5666	849.726	12.004	...	-391.9	...
N II 5666	850.733	12.004	...	-391.5	...
N II 5666	851.719	12.005	...	-370.0	...
N II 5666	852.742	12.005	...	-362.7	...
N II 5666	853.728	12.006	...	-352.9	...

Table 2—Continued

Ion / Line	HJD -2,454,000	Phase	W_λ (Å)	V_{\min} (km s ⁻¹)	V_b (km s ⁻¹)
N II 5666	854.740	12.006	...	-320.7	...
N II 5666	855.736	12.007	...	-299.3	...
N II 5666	857.786	12.008	...	-260.9	...
N II 5666	858.768	12.008	...	-254.7	...
N II 5666	859.775	12.009	...	-243.6	...
N II 5666	861.727	12.010	...	-226.4	...
N II 5666	862.739	12.010	...	-219.3	...
N II 5666	863.759	12.011	...	-224.5	...
N II 5666	864.728	12.011	...	-228.2	...
N II 5666	865.703	12.011	...	-208.3	...
N II 5666	866.717	12.012	...	-229.5	...
N II 5666	867.708	12.012	...	-222.0	...
N II 5666	875.652	12.016	...	-252.5	...
N II 5666	879.661	12.018	...	-257.7	...
N II 5666	880.672	12.019	...	-261.8	...
N II 5666	881.668	12.019	...	-262.7	...
N II 5676	755.860	11.957	...	-476.5	...
N II 5676	784.858	11.972	...	-460.5	...
N II 5676	818.806	11.988	...	-450.5	...
N II 5676	819.811	11.989	...	-450.4	...
N II 5676	821.852	11.990	...	-449.4	...
N II 5676	824.754	11.991	...	-455.5	...
N II 5676	829.784	11.994	...	-459.6	...
N II 5676	831.753	11.995	...	-464.1	...
N II 5676	836.751	11.997	...	-464.4	...
N II 5676	836.738	11.997	...	-470.8	...
N II 5676	837.732	11.998	...	-461.7	...
N II 5676	838.757	11.998	...	-458.8	...
N II 5676	839.787	11.999	...	-459.1	...
N II 5676	840.779	11.999	...	-455.6	...

Table 2—Continued

Ion / Line	HJD -2,454,000	Phase	W_λ (Å)	V_{\min} (km s ⁻¹)	V_b (km s ⁻¹)
N II 5676	841.768	12.000	...	-444.5	...
N II 5676	842.774	12.000	...	-445.1	...
N II 5676	843.774	12.001	...	-435.5	...
N II 5676	844.776	12.001	...	-433.1	...
N II 5676	845.765	12.002	...	-422.4	...
N II 5676	846.770	12.002	...	-414.8	...
N II 5676	847.797	12.003	...	-411.2	...
N II 5676	848.741	12.003	...	-418.2	...
N II 5676	849.726	12.004	...	-428.6	...
N II 5676	850.733	12.004	...	-442.0	...
N II 5676	851.719	12.005	...	-436.8	...
N II 5676	852.742	12.005	...	-441.0	...
N II 5676	853.728	12.006	...	-436.3	...
N II 5676	854.740	12.006	...	-459.4	...
N II 5676	855.736	12.007	...	-462.8	...
N II 5711	755.860	11.957	...	-314.1	...
N II 5711	784.858	11.972	...	-397.8	...
N II 5711	818.806	11.988	...	-384.4	...
N II 5711	819.811	11.989	...	-379.4	...
N II 5711	821.852	11.990	...	-380.1	...
N II 5711	824.754	11.991	...	-401.7	...
N II 5711	829.784	11.994	...	-395.3	...
N II 5711	831.753	11.995	...	-390.5	...
N II 5711	836.751	11.997	...	-422.0	...
N II 5711	836.738	11.997	...	-403.1	...
N II 5711	837.732	11.998	...	-427.4	...
N II 5711	838.757	11.998	...	-446.3	...
N II 5711	839.787	11.999	...	-431.3	...
N II 5711	840.779	11.999	...	-448.3	...
N II 5711	841.768	12.000	...	-448.1	...

Table 2—Continued

Ion / Line	HJD -2,454,000	Phase	W_λ (Å)	V_{\min} (km s ⁻¹)	V_b (km s ⁻¹)
N II 5711	842.774	12.000	...	-440.8	...
N II 5711	843.774	12.001	...	-450.4	...
N II 5711	844.776	12.001	...	-468.4	...
N II 5711	845.765	12.002	...	-443.7	...
N II 5711	846.770	12.002	...	-429.8	...
N II 5711	847.797	12.003	...	-425.3	...
N II 5711	848.741	12.003	...	-424.0	...
N II 5711	849.726	12.004	...	-404.8	...
N II 5711	850.733	12.004	...	-409.9	...
N II 5711	851.719	12.005	...	-391.8	...
N II 5711	852.742	12.005	...	-388.0	...
N II 5711	853.728	12.006	...	-367.3	...
N II 5711	854.740	12.006	...	-341.9	...
N II 5711	855.736	12.007	...	-350.5	...
N II 5711	857.786	12.008	...	-257.9	...
N II 5711	858.768	12.008	...	-253.8	...
N II 5711	859.775	12.009	...	-262.1	...
N II 5711	861.727	12.010	...	-256.1	...
N II 5711	862.739	12.010	...	-221.8	...
N II 5711	863.759	12.011	...	-243.2	...
N II 5711	864.728	12.011	...	-250.8	...
N II 5711	865.703	12.011	...	-226.7	...
N II 5711	866.717	12.012	...	-246.0	...
N II 5711	867.708	12.012	...	-247.1	...
N II 5711	875.652	12.016	...	-269.1	...
N II 5711	879.661	12.018	...	-281.2	...
N II 5711	880.672	12.019	...	-280.4	...
N II 5711	881.668	12.019	...	-282.5	...
Si II 6347	755.860	11.957	1.64	-569.1	...
Si II 6347	784.858	11.972	-0.28	-544.3	-72.4

Table 2—Continued

Ion / Line	HJD -2,454,000	Phase	W_λ (Å)	V_{\min} (km s ⁻¹)	V_b (km s ⁻¹)
Si II 6347	818.806	11.988	-1.77	-975.0	-147.1
Si II 6347	819.811	11.989	-2.01	-733.6	-150.9
Si II 6347	821.852	11.990	-1.58	-670.0	-149.6
Si II 6347	824.754	11.991	-1.72	-712.8	-334.4
Si II 6347	829.784	11.994	-1.79	-932.2	-148.7
Si II 6347	831.753	11.995	-1.73	-665.4	-157.1
Si II 6347	836.751	11.997	-1.77	-963.6	-168.5
Si II 6347	836.738	11.997	-1.05	-567.8	-159.3
Si II 6347	837.732	11.998	-1.77	-585.7	-138.0
Si II 6347	838.757	11.998	-1.27	-639.2	-144.7
Si II 6347	839.787	11.999	-1.69	-603.9	-158.4
Si II 6347	840.779	11.999	-1.18	-535.9	-151.6
Si II 6347	842.774	12.000	-0.93	-521.2	-133.8
Si II 6347	843.774	12.001	-0.99	-523.0	-107.8
Si II 6347	844.776	12.001	-0.82	-499.7	-87.5
Si II 6347	845.765	12.002	-1.82	-504.3	-81.6
Si II 6347	846.770	12.002	-1.20	-492.5	-52.6
Si II 6347	848.741	12.003	0.10	-491.3	-59.0
Si II 6347	849.726	12.004	-0.34	-490.3	-41.7
Si II 6347	850.733	12.004	-0.35	-480.4	-47.5
Si II 6347	851.719	12.005	-0.48	-473.4	-27.2
Si II 6347	852.742	12.005	-0.38	-468.1	-41.2
Si II 6347	853.728	12.006	-0.61	-457.2	-34.2
Si II 6347	854.740	12.006	-0.28	-459.7	-37.4
Si II 6347	855.736	12.007	-0.92	-452.0	-33.3
Si II 6347	857.786	12.008	-0.33	-442.3	-38.2
Si II 6347	858.768	12.008	-0.67	-434.2	-14.6
Si II 6347	859.775	12.009	0.26	-434.3	-14.7
Si II 6347	861.727	12.010	-0.39	-423.3	-6.5
Si II 6347	862.739	12.010	-0.40	-426.6	-11.3

Table 2—Continued

Ion / Line	HJD -2,454,000	Phase	W_λ (Å)	V_{\min} (km s ⁻¹)	V_b (km s ⁻¹)
Si II 6347	863.759	12.011	-0.62	-422.9	-0.8
Si II 6347	864.728	12.011	-0.15	-426.0	67.9
Si II 6347	866.717	12.012	-0.62	-414.4	56.9
Si II 6347	867.708	12.012	-0.16	-414.5	59.6
Si II 6347	875.652	12.016	-0.46	-399.0	58.7
Si II 6347	879.661	12.018	-0.57	-395.4	60.5
Si II 6371	755.860	11.957	...	-309.1	...
Si II 6371	784.858	11.972	...	-589.3	...
Si II 6371	818.806	11.988	...	-320.2	...
Si II 6371	819.811	11.989	...	-690.5	...
Si II 6371	821.852	11.990	...	-308.3	...
Si II 6371	824.754	11.991	...	-303.9	...
Si II 6371	829.784	11.994	...	-306.2	...
Si II 6371	831.753	11.995	...	-307.2	...
Si II 6371	836.751	11.997	...	-311.0	...
Si II 6371	836.738	11.997	...	-311.0	...
Si II 6371	837.732	11.998	...	-309.8	...
Si II 6371	838.757	11.998	...	-309.4	...
Si II 6371	839.787	11.999	...	-309.7	...
Si II 6371	840.779	11.999	...	-314.3	...
Si II 6371	842.774	12.000	...	-309.6	...
Si II 6371	843.774	12.001	...	-554.9	...
Si II 6371	844.776	12.001	...	-533.2	...
Si II 6371	845.765	12.002	...	-524.8	...
Si II 6371	846.770	12.002	...	-520.8	...
Si II 6371	848.741	12.003	...	-513.4	...
Si II 6371	849.726	12.004	...	-517.2	...
Si II 6371	850.733	12.004	...	-504.6	...
Si II 6371	851.719	12.005	...	-500.2	...
Si II 6371	852.742	12.005	...	-491.2	...

Table 2—Continued

Ion / Line	HJD -2,454,000	Phase	W_λ (Å)	V_{\min} (km s ⁻¹)	V_b (km s ⁻¹)
Si II 6371	853.728	12.006	...	-484.4	...
Si II 6371	854.740	12.006	...	-481.2	...
Si II 6371	855.736	12.007	...	-479.4	...
Si II 6371	857.786	12.008	...	-469.9	...
Si II 6371	858.768	12.008	...	-471.4	...
Si II 6371	859.775	12.009	...	-466.7	...
Si II 6371	861.727	12.010	...	-457.8	...
Si II 6371	862.739	12.010	...	-458.9	...
Si II 6371	863.759	12.011	...	-458.0	...
Si II 6371	864.728	12.011	...	-454.1	...
Si II 6371	866.717	12.012	...	-450.5	...
Si II 6371	867.708	12.012	...	-449.8	...
Si II 6371	875.652	12.016	...	-451.9	...
Si II 6371	879.661	12.018	...	-453.1	...
Fe II 5169	755.860	11.957	-26.86	-450.5	-321.2
Fe II 5169	784.858	11.972	-30.42	-443.2	-320.3
Fe II 5169	818.806	11.988	-26.25	-457.2	-324.1
Fe II 5169	819.811	11.989	-24.38	-458.5	-316.7
Fe II 5169	821.852	11.990	-25.34	-458.2	-316.7
Fe II 5169	824.754	11.991	-25.73	-457.6	-316.6
Fe II 5169	829.784	11.994	-25.24	-460.4	-318.3
Fe II 5169	831.753	11.995	-24.80	-460.4	-315.4
Fe II 5169	836.751	11.997	-24.63	-462.0	-312.6
Fe II 5169	836.738	11.997	-23.95	-463.7	-313.9
Fe II 5169	837.732	11.998	-24.15	-463.2	-312.2
Fe II 5169	838.757	11.998	-24.11	-466.0	-312.0
Fe II 5169	839.787	11.999	-24.47	-469.1	-312.3
Fe II 5169	840.779	11.999	-24.06	-468.8	-316.3
Fe II 5169	841.768	12.000	-22.96	-473.8	-311.2
Fe II 5169	842.774	12.000	-23.30	-474.5	-313.9

Table 2—Continued

Ion / Line	HJD -2,454,000	Phase	W_λ (\AA)	V_{\min} (km s^{-1})	V_b (km s^{-1})
Fe II 5169	843.774	12.001	-22.81	-478.6	-311.7
Fe II 5169	844.776	12.001	-21.60	-481.1	-307.3
Fe II 5169	845.765	12.002	-21.79	-482.2	-307.9
Fe II 5169	846.770	12.002	-21.90	-483.4	-306.4
Fe II 5169	847.797	12.003	-21.14	-483.9	-308.2
Fe II 5169	848.741	12.003	-21.08	-482.5	-301.6
Fe II 5169	849.726	12.004	-20.40	-485.0	-306.7
Fe II 5169	850.733	12.004	-21.08	-485.0	-305.6
Fe II 5169	851.719	12.005	-21.35	-484.8	-304.4
Fe II 5169	852.742	12.005	-21.34	-485.5	-303.3
Fe II 5169	853.728	12.006	-21.53	-482.9	-299.6
Fe II 5169	854.740	12.006	-21.68	-482.6	-304.3
Fe II 5169	855.736	12.007	-22.11	-481.2	-301.6
Fe II 5169	857.786	12.008	-22.59	-481.3	-300.9
Fe II 5169	858.768	12.008	-23.09	-480.4	-299.9
Fe II 5169	859.775	12.009	-23.35	-479.8	-302.0
Fe II 5169	861.727	12.010	-23.92	-478.2	-298.4
Fe II 5169	862.739	12.010	-23.10	-478.1	-301.5
Fe II 5169	863.759	12.011	-23.47	-478.6	-301.9
Fe II 5169	864.728	12.011	-21.61	-459.9	-289.5
Fe II 5169	865.703	12.011	-23.65	-478.1	-296.3
Fe II 5169	866.717	12.012	-22.87	-476.3	-300.1
Fe II 5169	867.708	12.012	-23.11	-476.6	-302.9
Fe II 5169	875.652	12.016	-21.84	-474.0	-306.6
Fe II 5169	879.661	12.018	-21.77	-474.2	-304.4
Fe II 5169	880.672	12.019	-21.94	-472.5	-304.0
Fe II 5169	881.668	12.019	-21.09	-473.0	-307.2
Fe II 5197	755.860	11.957	-3.28	-465.0	...
Fe II 5197	784.858	11.972	-1.92	-459.1	...
Fe II 5197	818.806	11.988	-3.78	-486.0	...

Table 2—Continued

Ion / Line	HJD -2,454,000	Phase	W_λ (\AA)	V_{\min} (km s^{-1})	V_b (km s^{-1})
Fe II 5197	819.811	11.989	-3.36	-514.6	...
Fe II 5197	821.852	11.990	-3.05	-489.2	...
Fe II 5197	824.754	11.991	-3.47	-536.6	...
Fe II 5197	829.784	11.994	-3.42	-573.6	...
Fe II 5197	831.753	11.995	-3.08	-493.0	...
Fe II 5197	836.751	11.997	-3.32	-529.5	...
Fe II 5197	836.738	11.997	-3.30	-560.3	...
Fe II 5197	837.732	11.998	-3.16	-511.7	...
Fe II 5197	838.757	11.998	-3.04	-509.5	...
Fe II 5197	839.787	11.999	-3.15	-503.2	...
Fe II 5197	840.779	11.999	-3.35	-513.2	...
Fe II 5197	841.768	12.000	-3.08	-507.2	...
Fe II 5197	842.774	12.000	-3.15	-502.7	...
Fe II 5197	843.774	12.001	-3.14	-514.6	...
Fe II 5197	844.776	12.001	-3.12	-529.5	...
Fe II 5197	845.765	12.002	-3.21	-519.2	...
Fe II 5197	846.770	12.002	-3.13	-509.5	...
Fe II 5197	847.797	12.003	-3.07	-502.2	...
Fe II 5197	848.741	12.003	-3.04	-505.3	...
Fe II 5197	849.726	12.004	-3.27	-507.0	...
Fe II 5197	850.733	12.004	-3.25	-510.0	...
Fe II 5197	851.719	12.005	-3.21	-504.0	...
Fe II 5197	852.742	12.005	-3.30	-505.2	...
Fe II 5197	853.728	12.006	-3.37	-497.9	...
Fe II 5197	854.740	12.006	-3.42	-497.3	...
Fe II 5197	855.736	12.007	-3.39	-495.4	...
Fe II 5197	857.786	12.008	-3.59	-497.9	...
Fe II 5197	858.768	12.008	-3.46	-494.4	...
Fe II 5197	859.775	12.009	-3.58	-489.5	...
Fe II 5197	861.727	12.010	-3.50	-489.3	...

Table 2—Continued

Ion / Line	HJD -2,454,000	Phase	W_λ (\AA)	V_{\min} (km s^{-1})	V_b (km s^{-1})
Fe II 5197	862.739	12.010	-3.31	-484.8	...
Fe II 5197	863.759	12.011	-3.44	-485.8	...
Fe II 5197	864.728	12.011	-2.50	-458.1	...
Fe II 5197	865.703	12.011	-3.31	-482.0	...
Fe II 5197	866.717	12.012	-3.23	-480.9	...
Fe II 5197	867.708	12.012	-3.09	-479.1	...
Fe II 5197	875.652	12.016	-2.65	-474.4	...
Fe II 5197	879.661	12.018	-2.54	-478.3	...
Fe II 5197	880.672	12.019	-2.40	-475.3	...
Fe II 5197	881.668	12.019	-2.32	-481.8	...
Fe II 5234	755.860	11.957	-3.46	-584.0	...
Fe II 5234	784.858	11.972	-1.36	-537.7	...
Fe II 5234	818.806	11.988	-3.34	-428.5	...
Fe II 5234	819.811	11.989	-3.06	-468.6	...
Fe II 5234	821.852	11.990	-3.23	-471.8	...
Fe II 5234	824.754	11.991	-3.16	-560.7	...
Fe II 5234	829.784	11.994	-2.89	-586.7	...
Fe II 5234	831.753	11.995	-3.01	-490.7	...
Fe II 5234	836.751	11.997	-3.10	-538.2	...
Fe II 5234	836.738	11.997	-3.03	-557.7	...
Fe II 5234	837.732	11.998	-3.00	-574.9	...
Fe II 5234	838.757	11.998	-3.16	-539.1	...
Fe II 5234	839.787	11.999	-3.07	-521.1	...
Fe II 5234	840.779	11.999	-3.04	-574.3	...
Fe II 5234	841.768	12.000	-2.76	-573.2	...
Fe II 5234	842.774	12.000	-3.03	-546.0	...
Fe II 5234	843.774	12.001	-2.99	-541.7	...
Fe II 5234	844.776	12.001	-2.58	-556.7	...
Fe II 5234	845.765	12.002	-2.90	-539.4	...
Fe II 5234	846.770	12.002	-2.97	-534.4	...

Table 2—Continued

Ion / Line	HJD -2,454,000	Phase	W_λ (\AA)	V_{\min} (km s^{-1})	V_b (km s^{-1})
Fe II 5234	847.797	12.003	-2.65	-552.8	...
Fe II 5234	848.741	12.003	-2.79	-500.5	...
Fe II 5234	849.726	12.004	-2.68	-545.6	...
Fe II 5234	850.733	12.004	-2.76	-532.6	...
Fe II 5234	851.719	12.005	-2.68	-530.1	...
Fe II 5234	852.742	12.005	-2.89	-518.0	...
Fe II 5234	853.728	12.006	-2.68	-509.1	...
Fe II 5234	854.740	12.006	-3.01	-517.2	...
Fe II 5234	855.736	12.007	-2.77	-507.2	...
Fe II 5234	857.786	12.008	-3.13	-498.7	...
Fe II 5234	858.768	12.008	-3.00	-500.4	...
Fe II 5234	859.775	12.009	-3.10	-494.5	...
Fe II 5234	861.727	12.010	-2.60	-487.7	...
Fe II 5234	862.739	12.010	-2.93	-491.7	...
Fe II 5234	863.759	12.011	-3.10	-485.9	...
Fe II 5234	864.728	12.011	-2.24	-446.4	...
Fe II 5234	865.703	12.011	-2.54	-478.9	...
Fe II 5234	866.717	12.012	-2.99	-477.4	...
Fe II 5234	867.708	12.012	-2.75	-473.4	...
Fe II 5234	875.652	12.016	-2.47	-474.3	...
Fe II 5234	879.661	12.018	-2.29	-481.9	...
Fe II 5234	880.672	12.019	-2.11	-469.8	...
Fe II 5234	881.668	12.019	-2.29	-465.1	...
Fe II 5316	755.860	11.957	-47.92	-547.3	33.9
Fe II 5316	784.858	11.972	...	-683.2	35.4
Fe II 5316	818.806	11.988	-7.97	-573.5	7.1
Fe II 5316	819.811	11.989	-7.70	-592.8	11.6
Fe II 5316	821.852	11.990	-8.03	-631.0	10.4
Fe II 5316	824.754	11.991	-9.02	-580.2	8.0
Fe II 5316	829.784	11.994	-8.80	-583.4	2.8

Table 2—Continued

Ion / Line	HJD -2,454,000	Phase	W_λ (Å)	V_{\min} (km s ⁻¹)	V_b (km s ⁻¹)
Fe II 5316	831.753	11.995	-8.63	-587.3	-1.3
Fe II 5316	836.751	11.997	-8.25	-592.1	2.6
Fe II 5316	837.732	11.998	-8.72	-599.8	2.4
Fe II 5316	838.757	11.998	-8.55	-579.3	-2.2
Fe II 5316	839.787	11.999	-8.75	-604.2	-0.1
Fe II 5316	840.779	11.999	-8.55	-578.7	5.2
Fe II 5316	841.768	12.000	-8.50	-570.5	1.0
Fe II 5316	842.774	12.000	-8.14	-570.4	2.5
Fe II 5316	843.774	12.001	-8.56	-563.0	-0.7
Fe II 5316	844.776	12.001	-8.53	-559.3	3.2
Fe II 5316	845.765	12.002	-8.10	-554.3	5.1
Fe II 5316	846.770	12.002	-8.52	-548.5	5.1
Fe II 5316	847.797	12.003	-7.21	-543.3	4.2
Fe II 5316	848.741	12.003	-7.88	-524.2	10.5
Fe II 5316	849.726	12.004	-7.87	-541.8	6.3
Fe II 5316	850.733	12.004	-7.92	-535.8	8.6
Fe II 5316	851.719	12.005	-7.74	-527.5	10.9
Fe II 5316	852.742	12.005	-7.92	-529.5	12.4
Fe II 5316	853.728	12.006	-7.09	-520.1	17.7
Fe II 5316	854.740	12.006	-7.24	-521.2	15.5
Fe II 5316	855.736	12.007	-7.72	-522.4	17.7
Fe II 5316	857.786	12.008	-8.23	-517.2	19.5
Fe II 5316	858.768	12.008	-8.24	-516.3	19.9
Fe II 5316	859.775	12.009	-8.04	-514.5	17.5
Fe II 5316	861.727	12.010	-7.76	-508.1	20.6
Fe II 5316	862.739	12.010	-8.17	-511.2	20.9
Fe II 5316	863.759	12.011	-7.78	-510.5	19.0
Fe II 5316	864.728	12.011	...	-476.8	56.9
Fe II 5316	865.703	12.011	-7.28	-510.2	19.0
Fe II 5316	866.717	12.012	-7.31	-507.0	22.3

Table 2—Continued

Ion / Line	HJD -2,454,000	Phase	W_λ (\AA)	V_{\min} (km s^{-1})	V_b (km s^{-1})
Fe II 5316	867.708	12.012	-7.05	-508.9	18.6
Fe II 5316	875.652	12.016	-6.30	-503.3	16.4
Fe II 5316	879.661	12.018	-6.37	-511.4	15.7
Fe II 5316	880.672	12.019	-6.43	-512.2	15.7
Fe II 5316	881.668	12.019	-6.15	-511.9	12.8
Fe II 6248	755.860	11.957	...	-465.1	...
Fe II 6248	784.858	11.971	...	-452.0	...
Fe II 6248	818.806	11.988	...	-464.3	...
Fe II 6248	819.811	11.989	...	-467.2	...
Fe II 6248	821.852	11.990	...	-463.2	...
Fe II 6248	824.754	11.991	...	-467.1	...
Fe II 6248	829.784	11.994	...	-461.1	...
Fe II 6248	831.753	11.995	...	-465.0	...
Fe II 6248	836.751	11.997	...	-457.2	...
Fe II 6248	836.738	11.997	...	-286.1	...
Fe II 6248	837.732	11.998	...	-263.0	...
Fe II 6248	838.757	11.998	...	-283.2	...
Fe II 6248	839.787	11.999	...	-264.9	...
Fe II 6248	840.779	11.999	...	-272.3	...
Fe II 6248	841.768	12.000	...	-287.4	...
Fe II 6248	842.774	12.000	...	-679.8	...
Fe II 6248	843.774	12.001	...	-669.8	...
Fe II 6248	844.776	12.001	...	-635.1	...
Fe II 6248	845.765	12.002	...	-640.7	...
Fe II 6248	846.770	12.002	...	-621.6	...
Fe II 6248	847.797	12.003	...	-608.6	...
Fe II 6248	848.741	12.003	...	-610.1	...
Fe II 6248	849.726	12.004	...	-612.0	...
Fe II 6248	850.733	12.004	...	-589.5	...
Fe II 6248	851.719	12.005	...	-582.5	...

Table 2—Continued

Ion / Line	HJD -2,454,000	Phase	W_λ (Å)	V_{\min} (km s ⁻¹)	V_b (km s ⁻¹)
Fe II 6248	852.742	12.005	...	-569.6	...
Fe II 6248	853.728	12.006	...	-553.4	...
Fe II 6248	854.740	12.006	...	-572.1	...
Fe II 6248	855.736	12.007	...	-543.2	...
Fe II 6248	857.786	12.008	...	-560.6	...
Fe II 6248	858.768	12.008	...	-554.3	...
Fe II 6248	859.775	12.009	...	-542.5	...
Fe II 6248	861.727	12.010	...	-529.3	...
Fe II 6248	862.739	12.010	...	-532.2	...
Fe II 6248	863.759	12.011	...	-525.7	...
Fe II 6248	864.728	12.011	...	-457.0	...
Fe II 6248	865.703	12.011	...	-503.8	...
Fe II 6248	866.717	12.012	...	-533.9	...
Fe II 6248	867.708	12.012	...	-531.9	...
Fe II 6248	875.652	12.016	...	-618.2	...
Fe II 6248	881.668	12.019	...	-708.4	...